Study of excitons in gapped graphene and of the influence of hole geometry on the band gap of graphene antidot lattices

Project written

by

René Petersen

10. Semester Nano-Physics Student

aauprojects@repetit.dk

June 17, 2009

Supervisor:
Ph. D., Professor, Thomas Garm Pedersen

Aalborg University
Faculty of Engineering and Science
Institute of Physics and Nanotechnology

Abstract

Excitonic binding energies in graphene antidot lattices are calculated using the Wannier model with the effective mass approximation. The screening is determined by solving the Poisson equation for the two interface system air-graphene-SiO_2 and calculating the dielectric function of the graphene layer itself by employing a two band model of gapped graphene. An expression for the binding energy which depends on the thickness of the graphene layer is obtained and it is found that the exciton binding energy is almost independent of the layer thickness. Choosing the graphene lattice constant $a_{cc} = 1.42$Å as the layer thickness it is found that the binding energies are reduced by a factor of ≈ 2.6 compared to the much simpler model applied in [1] and [2].

Furthermore, exciton binding energies are calculated using the Wannier model with linear bands. This is more appropriate to graphene. It is found that the linear band model increases the binding energy and thereby makes the electron and the hole more tightly bound. In some cases the binding energy diverges which is probably due to limitations in the variational approach used.

In addition, antidot lattices in which the holes are placed in a rectangular lattice are investigated and compared to the hexagonal antidot lattices. It is found that the presence of a gap is highly dependent on the details of the structure and that only structures for which the unit cell width obeys the rule $L_y = 3 + 2n$ ($n = 1, 2...$), with the width measured in the armchair direction, have an appreciable band gap. Furthermore, in the case of hexagonal lattices the gap is always located at the Γ point in the Brillouin zone, however, for different rectangular lattices the gap moves around the Brillouin zone and might even be located between two high symmetry points.

Preface

This work has been carried out during the period 1. Feb 2009 - 17. Jun 2009 and it constitutes the thesis for my master degree in nanophysics. It is a continuation of a previous work on graphene antidot lattices. Both this work and the previous work can be found at www.repetit.dk. Although this work builds upon the results from a previous work, it can be read independently. Some of the most important prerequisites are given in the introduction, but additional information can be found in the appendices.

The software used for numerical calculations has been written using the Intel Fortran compiler version 11.0.072 and the Intel Math Kernel Library (Intel MKL) version 10.1.025.

Throughout the text vectors are typeset as $\boldsymbol{a}$, matrices as $\hat{A}$ and operators as $\hat{A}$. Most of the time matrices are written in uppercase and vectors in lowercase. Complex quantities and Fourier transforms/coefficients are denoted with a tilde like $\tilde{\sigma}$.

The first chapter provides an introduction to graphene and graphene antidot lattices and it presents the results from the previous work that this work builds upon. The chapter "Screening in gapped graphene" explains the theory behind the model applied for the calculation of the exciton binding energies. An appendix is provided in order to give further details on the calculation of the conductivity. The next chapter "Wannier model of excitons" explains the theory behind excitons and how the excitonic binding energies can be calculated. "Implementation and results" presents and discusses the results obtained. The final chapter concludes on the results.

During the work on this thesis an article on quasi-particle effects in hexagonal antidot lattices has been submitted for publication [1].

I would like to thank my supervisor, Professor, Thomas Garm Pedersen, for being very helpful and motivating throughout my work on this thesis.

<div align="center">

_____

René Petersen

</div>

Contents

Chapter 1

Introduction

1.1 The discovery of graphene

Graphene is a two dimensional one atom thick planar sheet of sp^2 bonded carbon atoms densely packed in a honeycomb structure. It is the building block of graphite, which consists of planes of graphene stacked on top of each other. Carbon nanotubes and fullerenes can be thought of as rolled up graphene sheets, so that graphene constitutes the basic building block of many carbon allotropes. Graphene has shown superior electrical and mechanical properties with a mobility on the order of $200000 \, \mathrm{cm}^2/(\mathrm{Vs})$ [3] and a Young's Modulus of $500 \, \mathrm{GPa}$. For comparison, silicon has an electron mobility of $1350 \, \mathrm{cm}^2/(\mathrm{Vs})$ and carbon nanotubes has a Young's Modulus of $1000 \, \mathrm{GPa}$. The high mobility makes ballistic transport over distances on the order of micrometers possible [3].

<div align="center">(a)   (b)</div>
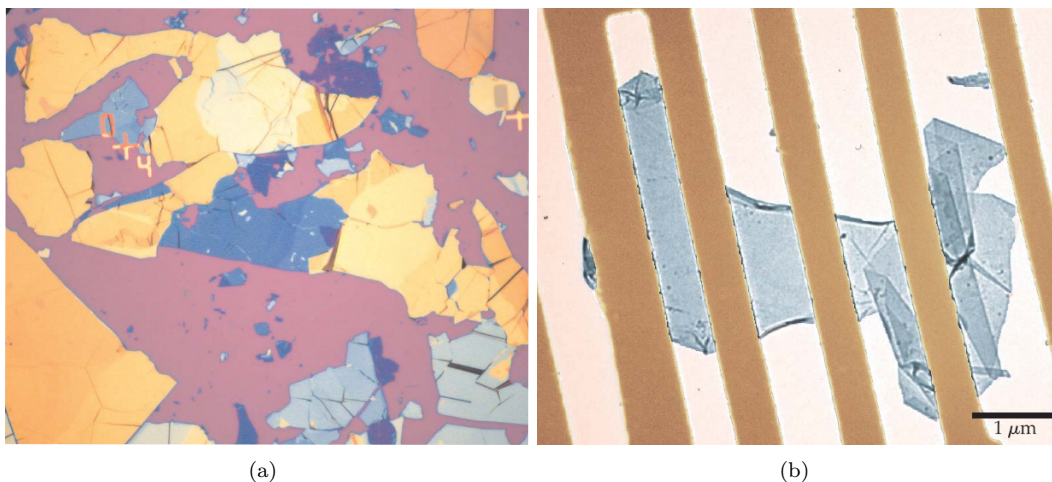
Figure 1.1: (a) Graphene flakes placed on an SiO_2 wafer and viewed in an optical microscope. Monolayers can be found by searching for flakes which show the weakest contrast and examining them by AFM. (b) A TEM image of graphene layers hanging freely on a scaffold of gold wires. [4]

Graphene is probably the best theoretically studied carbon allotrope. It is the starting point for

all calculations on carbon nanotubes and fullerenes. It is therefore quite ironic that only until recently it was believed that graphene was impossible to synthesize. According to the Mermin-Wagner theorem, long range order in two dimensions are theoretically impossible [5]. Since graphene is a two dimensional crystal it should therefore not exist, and several attempts to synthesize graphene have failed. This is because thermal fluctuations at growth temperatures tend to twist and crumble otherwise flat nanometer scale graphene crystallites into stable 3D structures like nanotubes or fullerenes. In 2005 though, a group from Manchester University used a different and quite naive approach to the production of graphene [6]. By simply rubbing a 3D layered crystal against another solid surface they found that among the resulting flakes some single layer flakes were unexpectedly always found. The identification of the monolayers among the other flakes produced was done by optical microscopy. By placing the flakes on top of an oxidized silicon wafer the monolayers became visible because even the monolayers add up sufficiently to the optical path length so that the interference color changes with respect to the bare substrate. This can be seen in Fig. 1.1. These results show that graphene does in fact exist and is quite easy to produce, and they have triggered an enormous research activity.

Another and possibly even simpler method for graphene production is tape peeling. By putting a thin graphite sample onto adhesive tape, folding the tape back onto the graphite, so that the graphite becomes sandwiched in between, peeling the tape apart and repeating the process some 5-10 times, graphene layers can be produced [5]. The graphene layers can be subsequently transferred onto a silicon dioxide surface for identification and characterization.

In a simple nearest neighbour model graphene is a semimetal with zero overlap between valence and conduction bands. Graphene is peculiar in the respect that the bands are linear near the K points at the corners of the Brillouin zone (see App. C for more about the peculiar behaviour of graphene). In Fig. 1.2 the band structure of graphene is shown and the right part of the figure shows the linearly dispersive bands. This linear dispersion closely resembles the Dirac spectrum for massless fermions which is given by $E = c\hbar k$ where $k = |\boldsymbol{k}|$. The linear dispersion in graphene near the K points is given by $E = v_F \hbar k$ so that the Fermi velocity $v_F \approx 10^6$ plays the role of the speed of light. For these reasons the K points are also called the Dirac points.
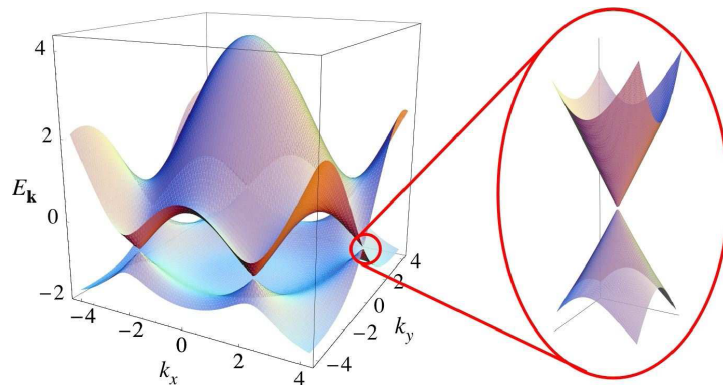
Figure 1.2: The band structure of graphene. The left part shows the whole band structure and the right part shows the linear dispersion around the dirac points. [7]

The surface to volume ratio of graphene is very large. Every atom is exposed on the surface and all atoms are therefore available for interaction with nearby molecules. This makes graphene very sensitive to changes in the local environment and its use as a sensor device is obvious.

The properties of graphene are metallic. If graphene is to be used as the main ingredient

in future transistors instead of silicon, a method to make graphene semiconducting has to be found. Inspired by the knowledge of carbon nanotubes (CNTs), the so called graphene nanoribbons (GNRs) have recently become an active area of research [8]. GNRs are unfolded carbon nanotubes and it is therefore reasonable to expect them to have some properties in common. Due to confinement of the electrons in CNTs some CNTs become semiconducting. When a CNT is unrolled the electrons are still confined to a small planar sheet and this causes some GNRs to be semiconducting too. In [8] and [9] it is demonstrated that the band gap of GNRs can be tuned by adjusting the GNR width. This opens up possibilities for using GNRs in electronic and optical applications.

Another approach to making graphene semiconducting is to introduce an additional periodic perturbation into the lattice. This can be done by making a periodic array of holes in the graphene sheet [10] [11] [2]. Due to this additional potential a gap opens up at the Γ point in the Brillouin zone. This gap can be tuned by adjusting the hole diameter and separation. In [10] and [11] a simple tight binding model with nearest neighbour interactions and no overlap of atomic wave functions has been used to determine electronic band structures and absorption spectra of a number of graphene antidot lattices. The next section is devoted to explaining the basic properties of graphene antidot lattices.

(a)   (b)
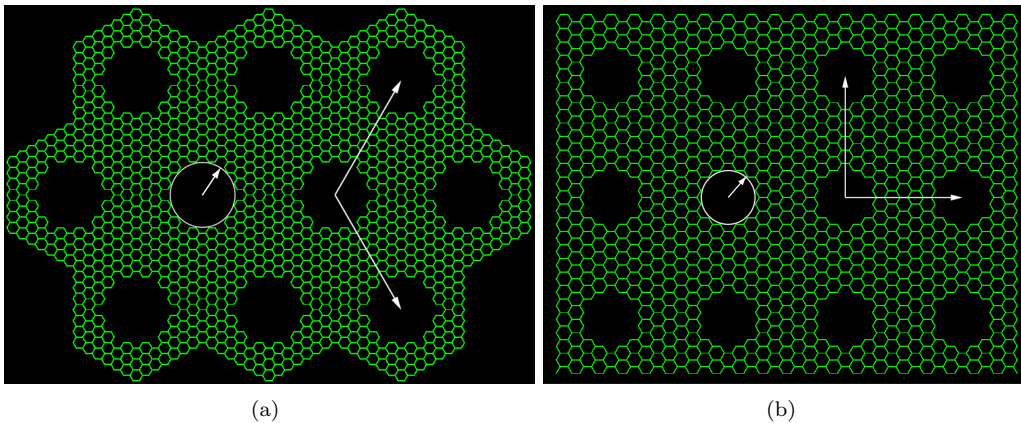
Figure 1.3: Super cell structure of (a) a hexagonal {7,3} antidot lattice and (b) a square {9,2} antidot lattice. The atoms within the white circles are removed to form the holes, and the arrow in the circles illustrates the hole radius.

1.2   Gapped graphene and graphene antidot lattices

As mentioned in the previous section graphene can be turned semiconducting by the introduction of a periodic array of holes into the graphene crystal. This is called a graphene antidot lattice, where the term antidot refers to the fact that the holes repel electrons in contrast to quantum dots which trap them. The antidot lattices are characterized by the following parameters

1. The geometry of the holes, i.e., are the holes arranged in a square lattice, hexagonal lattice, or some other lattice.

2. The size of the holes.

3. The distance between the holes.

4. Defects in the lattice, misplaced holes or missing holes.

In Fig. 1.3 two types of antidot lattices are shown. The left part of the figure shows a hexagonal lattice with a possible choice of lattice vectors. The designation {7,3} denotes the parameters of the hexagonal lattice. The first number refers to the edge length of the unit cell while the second number refers to the radius of the hole. In the right part of the figure a square antidot lattice is shown. Here the two parameters refer to the width of the unit cell and the radius of the hole. The actual setup of the antidot geometry will be explained in more detail later. At this point, what is important to know is that antidot lattices come in different geometries with different parameters and the size of the gap depends on these parameters.

In an earlier work [1] band structures and optical spectra of a number of graphene antidot lattices have been calculated in a nearest neighbour tight binding model (NN-TB), and in the quasi-particle model (QP-TB) of Grüneis et al. [12]. The nearest neighbour model reproduces the linear band structure with the correct slope in the vicinity of the Γ point, but it should be used with care in the rest of the Brillouin zone and for higher excited states. DFT calculations of band gaps and excited states underestimate the band gap and yield incorrect results for excited states. The QP-TB model employed includes quasi-particle effects into the calculations and these effects are known to be important in semiconductors. In Fig. 1.4 the band structures of two antidot lattices, {12,5} and {17,5}, are shown. These two structures represent intermediate and large structures, approaching what can be realized experimentally. The band structures show that the band gap increases by about 10% to 15% when using the QP-TB model instead of the NN-TB model, and this trend is seen for other antidot structures as well, at least when the ratio of removed atoms to total number of atoms (before any are removed to form the hole) is small, $N_{\text{rem}}^{1/2}/N_{\text{total}} \approx 0$. This is shown in Fig. 1.5, where it can also be seen that plotting the band gap versus this characteristic ratio yields an approximately linear relationship for small ratios.
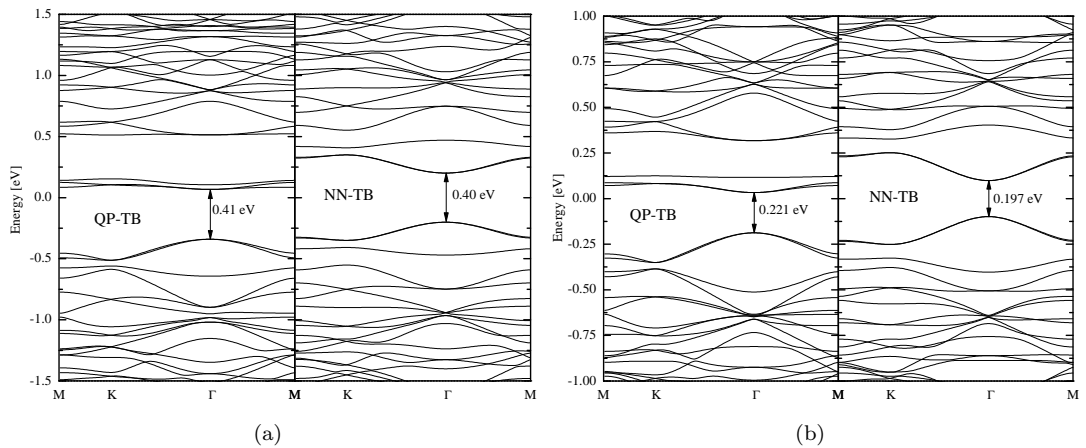
Figure 1.4: Band structures of (a) {12,5} and (b) {17,5} hexagonal antidot structures. The right part of each figure is calculated in a nearest neighbour tight binding model (NN-TB) while the left part is calculated in a quasi-particle tight binding model (QP-TB).

In Fig. 1.6 the absorbance spectra of hexagonal antidot lattices {10,x} and {12,x} are shown. The dash-dotted lines are NN-TB and the solid lines are QP-TB. From these spectra the
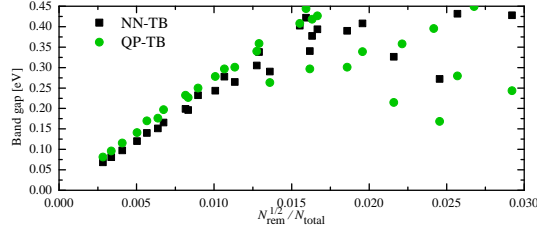
Figure 1.5: Plot of the band gap vs. $N_{rem}^{1/2}/N_{tot}$ for various antidot structures. The QP-TB band gaps generally lie higher than the NN-TB gaps when the ratio is small.

increase of the size of the band gap can also be seen since the absorption edge is shifted in the QP-TB model. In addition, it is seen that the quasi-particle corrections to the spectra are much more pronounced for structures with large holes compared to the size of the unit cell. Some spectra are barely even recognizable when using the QP-TB model and in some cases the band gap actually decreases in QP-TB.
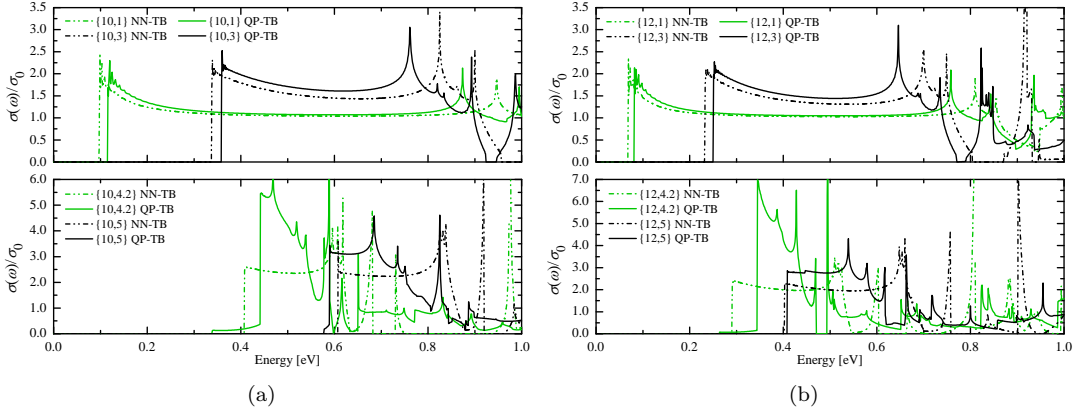
Figure 1.6: Real part of the conductivity ($Re[\tilde{\sigma}(\omega)]$, optical absorption) of (a) {10,x} antidot lattices and (b) {12,x} antidot lattices in both the nearest neighbour tight binding (NN-TB) and quasi-particle tight binding (QP-TB) model.

When an electron is excited into a conduction band state an empty electron state is left in the valence band. This empty electron state behaves like a positively charged electron with some effective mass, and can thus be viewed as being occupied by a positively charged "hole". The hole interacts with the excited electron through the Coulomb potential thus introducing energy states which are lower than those of the excited electron. The bound electron-hole pair moves through the crystal as a pair and can thus be viewed as a single particle. This particle is called an exciton. Due to excitonic effects additional energy states are introduced below the band gap. In the optical spectra excitonic effects should be seen as peaks below the absorption edge. Neither the QP-TB nor the NN-TB model employed here take excitons into account however, but using the simple Wannier model (this will be treated in more detail later), a simple estimate of the exciton binding energies can be made. In the Wannier model the exciton energy levels are give by

$$E_n = E_g - \frac{\text{Ry}^*}{(n + \frac{1}{2})^2}, \qquad \text{Ry}^* = 13.6[\text{eV}]\frac{\mu}{\varepsilon^2} \tag{1.1}$$

where E_g is the band gap, $n = 0, 1 \ldots$, and Ry^* is the effective screened Rydberg with μ the reduced exciton mass ($\mu = m_e m_h/(m_e + m_h)$) and ε the relative dielectric constant. The effective Rydbergs of some antidot lattices are given below

$$\text{Ry}^*_{\{5,1\}} = 55\,\text{meV} \qquad \text{Ry}^*_{\{5,3\}} = 574\,\text{meV} \qquad \text{Ry}^*_{\{10,1\}} = 13\,\text{meV}$$
$$\text{Ry}^*_{\{10,3\}} = 54\,\text{meV} \qquad \text{Ry}^*_{\{10,5\}} = 205.0\,\text{meV} \qquad \text{Ry}^*_{\{10,7\}} = 371.0\,\text{meV}$$

For the first exciton state, $n = 0$, the binding energy is given by $E_B = -4\text{Ry}^*$. This gives quite large binding energies for all antidot lattices, which is expected since the effect is large in graphene. For some antidot lattices however, the excitonic energy levels are negative. This does not seem reasonable, because it would actually make the exciton state the ground state. In employing the Wannier model some quite rough approximations have been made, and this is probably the source of these seemingly unphysical results.

1.3 The purpose of this project

This work is a continuation of previous work on graphene antidot lattices [2] [1], although it can be read independently. In the previous work hexagonal antidot lattices were treated and the band structures, optical spectra and excitonic energies presented above were calculated using a QP-TB (quasi-particle) tight binding model.

In [2] only antidot lattices with a hexagonal hole geometry have been investigated. Recently, square antidot lattices have been fabricated experimentally [13], however, with a much larger hole diameter and lattice constant than what it is possible to model numerically. It would however be exciting to model small square antidot lattices numerically to see if some agreement with the experimental results is seen. Thus, one of the main focuses of this work is to model square antidot lattices and compare them to hexagonal lattices and to the experimental data.

As mentioned above, in the previous work, excitonic binding energies in graphene antidot lattices have been determined based on the simple Wannier model. In the calculation of the effective Rydberg one needs the effective dielectric constant and the calculation of this is itself a complicated task. Therefore, the relative dielectric constant was calculated in a rather arbitrary way, by assuming that the screening in the graphene layer was determined only by the average of the screening in the surrounding media. Thus, with graphene on a silicon dioxide substrate surrounded by air, the average dielectric constant becomes $\varepsilon = 2.5$. This gave unphysical results for some lattices. The two most probable reasons for the failure of the model are as follows

1. The calculation of the relative dielectric constant does not take into account the presence of the graphene layer at all. It is based on the assumption that the very thin graphene layer does not contribute much to the screening itself, but this is a very crude assumption.

2. The Wannier model in itself. In deriving the results Eqn. 1.1 the effective mass approximation has been used. This approximation basically assumes that the bands are parabolic at the point of band gap, but in graphene antidot lattices the bands are only parabolic very close to the band gap and linear farther away from it.

The first of these reasons is the one which is expected to have the largest significance. Thus, two things need to be done. First, a model of the relative dielectric constant taking into account the presence of the graphene layer has to be made. Second, excitonic energies should be calculated using the linear energy dispersion near the band gap instead of a parabolic dispersion.

Chapter 2

Screening in gapped graphene

2.1 Screening in a two interface system

As mentioned in the introduction, the calculation of the exciton binding energies in graphene antidot lattices gave unphysical results in some cases when using a very simple estimate for the screening in the graphene layer. One of the main reasons for this is probably the quite naive calculation of the screening in the graphene layer, which did not take the graphene layer itself into account, but simply assumed that the screening was determined by the surroundings only. In this chapter a more satisfactory model of the screening is developed. The theory in this chapter is based upon [14].

In a thin layer of a material characterized by a dielectric constant ε situated in between two semi-infinite materials of dielectric constants ε_a and ε_b, the screening is determined by both ε of the thin layer itself and by ε_a and ε_b of the surrounding material. The geometry is illustrated in Fig. 2.1.
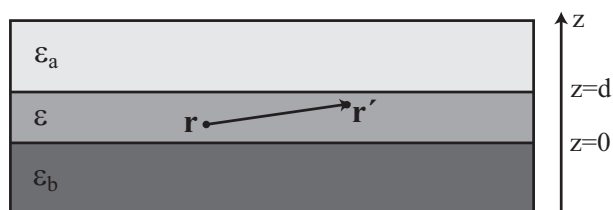
Figure 2.1: *Illustration of the geometry of a two interface system. The material characterized by ε is sandwiched between two other materials characterized by ε_a and ε_b. r and r' are the positions of two electrons in the middle layer.*

In order to determine the screening the interaction between two electrons located at $\boldsymbol{r}$ and $\boldsymbol{r}'$ in the middle layer is considered. The Poisson equation is then solved for this system to determine the interaction of an electron at $\boldsymbol{r}$ with another electron at $\boldsymbol{r}'$. From the resulting expression the screening can be deduced.

From Maxwell's equations $\boldsymbol{\nabla} \cdot (\varepsilon \boldsymbol{E}) = \rho/\varepsilon_0$ and from electrostatics the electric field is given by $\boldsymbol{E} = -\boldsymbol{\nabla}\phi$ so that

$$\boldsymbol{\nabla} \cdot [\varepsilon(\boldsymbol{r})\boldsymbol{\nabla}\phi] = \frac{-\rho}{\varepsilon_0} \tag{2.1}$$

where ϕ is the electrostatic potential. If ε is independent of $\boldsymbol{r}$ the usual Poisson equation $\nabla^2\phi = -\rho/(\varepsilon\varepsilon_0)$ is obtained. In the following, working with the potential energy U of an electron instead of the electrostatic potential is preferred, thus

$$\boldsymbol{\nabla} \cdot [\varepsilon(\boldsymbol{r})\boldsymbol{\nabla}U] = \frac{|e|\,\rho}{\varepsilon_0} \tag{2.2}$$

In the layer structure depicted in Fig. 2.1 the dielectric constant of the system changes only in the z-direction. The potential is Fourier decomposed in the x,y plane according to (see App. D)

$$U(\boldsymbol{r}, \boldsymbol{r}') = \frac{1}{2\pi}\int \tilde{U}(z, z'; q)e^{i\boldsymbol{q}\cdot(\boldsymbol{\rho}-\boldsymbol{\rho}')}d^2q \tag{2.3}$$

where $\boldsymbol{r} = (x, y, z)$ and $\boldsymbol{\rho} = (x, y)$ (the in-plane component) and similarly for the primed coordinates. The charge density at $\boldsymbol{r}$ due to an electron at $\boldsymbol{r}'$ is given by $\rho(\boldsymbol{r}, \boldsymbol{r}') = -|e|\,\delta(\boldsymbol{r} - \boldsymbol{r}') = -|e|\,\delta(x-x')\delta(y-y')\delta(z-z')$. Of course the true charge density in the thin film is further complicated by the other electrons, but it is assumed that these effects are included in the dielectric constant. Fourier decomposing also the charge density in the x,y plane one gets for the charge density

$$\rho(\boldsymbol{r}, \boldsymbol{r}') = -|e|\,\delta(z-z')\frac{1}{2\pi}\int e^{i\boldsymbol{q}\cdot(\boldsymbol{\rho}-\boldsymbol{\rho}')}d^2q \tag{2.4}$$

Inserting the decomposition of the potential into the Poisson equation one obtains for the left hand side

$$\boldsymbol{\nabla} \cdot \left[\varepsilon(\boldsymbol{r})\boldsymbol{\nabla}\frac{1}{2\pi}\int \tilde{U}(z, z'; q)e^{i\boldsymbol{q}\cdot(\boldsymbol{\rho}-\boldsymbol{\rho}')}d^2q\right] = \frac{1}{2\pi}\int \left\{\boldsymbol{\nabla} \cdot \left[\varepsilon(\boldsymbol{r})\boldsymbol{\nabla}\tilde{U}(z, z'; q)e^{i\boldsymbol{q}\cdot(\boldsymbol{\rho}-\boldsymbol{\rho}')}\right]\right\} d^2q \tag{2.5}$$

Using elementary vector calculus one arrives at (suppressing the dependence of ε and $\tilde{U}$ on $\boldsymbol{r}$, z, z' and q)

$$\frac{1}{2\pi}\int \left\{-q^2\varepsilon\tilde{U} + i\varepsilon\boldsymbol{q}\cdot\boldsymbol{\nabla}\tilde{U} + i\tilde{U}\boldsymbol{q}\cdot\boldsymbol{\nabla}\varepsilon + \varepsilon\nabla^2\tilde{U} + i\varepsilon\boldsymbol{q}\cdot\boldsymbol{\nabla}\tilde{U} + \boldsymbol{\nabla}\varepsilon\boldsymbol{\nabla}\tilde{U}\right\}e^{i\boldsymbol{q}\cdot(\boldsymbol{\rho}-\boldsymbol{\rho}')}d^2q$$

$$= \frac{1}{2\pi}\int \left\{-q^2\varepsilon\tilde{U} + \varepsilon\nabla^2\tilde{U} + \boldsymbol{\nabla}\varepsilon\boldsymbol{\nabla}\tilde{U}\right\}e^{i\boldsymbol{q}\cdot(\boldsymbol{\rho}-\boldsymbol{\rho}')}d^2q \tag{2.6}$$

for the left hand side of the Poisson equation. The last equality follows for the following reason: $\boldsymbol{\nabla}\tilde{U}$ and $\boldsymbol{\nabla}\varepsilon$ are always out of the plane because both $\tilde{U}$ and ε depend only on the spatial

coordinate z, therefore, since $\boldsymbol{q}$ is always in the plane, the second, third and fifth term in the above expression vanish. Inserting this and the Fourier decomposition of the charge density into the Poisson equation

$$\int \left\{ -q^2 \varepsilon \tilde{U} + \varepsilon \nabla^2 \tilde{U} + \boldsymbol{\nabla} \varepsilon \boldsymbol{\nabla} \tilde{U} \right\} e^{i\boldsymbol{q} \cdot (\boldsymbol{\rho} - \boldsymbol{\rho'})} d^2 q = \frac{-e^2 \delta(z - z')}{\varepsilon_0} \int e^{i\boldsymbol{q} \cdot (\boldsymbol{\rho} - \boldsymbol{\rho'})} d^2 q \tag{2.7}$$

Since this is essentially the Poisson equation with the potential and the charge density Fourier decomposed, it must of course be fulfilled everywhere in space. This means that the Fourier components on the left hand side must equal the Fourier components on the right hand side, and the following equation for the Fourier components is obtained

$$\left(q^2 \varepsilon - \varepsilon \nabla^2 - \boldsymbol{\nabla} \varepsilon \boldsymbol{\nabla} \right) \tilde{U} = \frac{e^2 \delta(z - z')}{\varepsilon_0} \tag{2.8}$$

Since ε (the screening in the system) and $\tilde{U}$ depends only on the z coordinate the following equation for the Fourier coefficients is obtained

$$\left(q^2 \varepsilon(z) - \varepsilon(z) \frac{d^2}{dz^2} - \frac{d}{dz} \varepsilon(z) \frac{d}{dz} \right) \tilde{U}(z, z'; q) = \frac{e^2 \delta(z - z')}{\varepsilon_0} \tag{2.9}$$

where the dependency of ε and $\tilde{U}$ on z, z' and q has been reintroduced. In order to solve this equation it is assumed that $0 \leq z' \leq d$, i.e., that the electron generating the potential is always situated in the layer characterized by ε. The equation is solved for the three layers separately. In the two layers $z > d$ and $z < 0$ the delta function vanish for all z so that only in the $0 \leq z \leq d$ layer does the delta function contribute. The solutions are of the following types

$$\tilde{U}(z, z'; q) = \begin{cases} Ae^{-qz} & z > d \\ Be^{qz} & z < 0 \\ Ce^{-q|z-z'|} + De^{-qz} + Fe^{qz} & 0 \leq z \leq d \end{cases} \tag{2.10}$$

The exponential function $e^{-q|z-z'|}$ gives a delta function when differentiated twice and thus takes care of the delta function on the right hand side of the equation for the coefficients. Since the potential has only been Fourier decomposed in the x,y plane the Fourier coefficients $\tilde{U}(z, z'; q)$ need to represent the potential $U(z, z')$ in the z-direction. Thus, the coefficients and the potential must have the same dependence on z and z'. Therefore, the boundary conditions which have to be fulfilled by the potential applies to the Fourier coefficients

$$\tilde{U}(d^-, z'; q) = \tilde{U}_a(d^+, z'; q) \tag{2.11}$$

$$\tilde{U}(0^+, z'; q) = \tilde{U}_b(0^-, z'; q) \tag{2.12}$$

$$\varepsilon(z) \frac{d\tilde{U}}{dz}\bigg|_{z=d^-} = \varepsilon_a \frac{d\tilde{U}_a}{dz}\bigg|_{z=d^+} \tag{2.13}$$

$$\varepsilon(z) \frac{d\tilde{U}}{dz}\bigg|_{z=0^+} = \varepsilon_b \frac{d\tilde{U}_b}{dz}\bigg|_{z=0^-} \tag{2.14}$$

Upon solving these equations expressions for the constants A, B, D and F in terms of C can be obtained. The constant C can be obtained by the requirement that the solution in the region $0 \leq z \leq d$ (Eqn. 2.10) has to be a solution to Eqn. 2.9. This gives

$$C = \frac{e^2}{2q\varepsilon\varepsilon_0} \tag{2.15}$$

The calculation of the constants A, B, D and F using the boundary conditions is relatively straightforward but tedious and is therefore not done here. Only the result for the Fourier coefficients is given

$$\tilde{U}(z, z'; q) = \frac{e^2}{2\varepsilon\varepsilon_0} \frac{e^{-q(z+z')}}{q} \frac{\left[e^{2qz_>}(\varepsilon - \varepsilon_a) + e^{2dq}(\varepsilon + \varepsilon_a)\right]\left[\varepsilon - \varepsilon_b + e^{2qz_<}(\varepsilon + \varepsilon_b)\right]}{e^{2dq}(\varepsilon + \varepsilon_a)(\varepsilon + \varepsilon_b) - (\varepsilon - \varepsilon_a)(\varepsilon - \varepsilon_b)} \tag{2.16}$$

where $z_> = \max(z, z')$ and $z_< = \min(z, z')$. This expression has been obtained by comparing the expression for $\tilde{U}(z, z'; q)$ when $z < z'$ and $z > z'$. If the two dimensional limit is taken, i.e., if both charges are placed at $z = d/2$, the following is obtained

$$\tilde{U}(d/2, d/2; q) = \frac{e^2}{2q\varepsilon\varepsilon_0} \frac{1}{\frac{\varepsilon_a - \varepsilon}{(\varepsilon_a + \varepsilon)e^{dq} - \varepsilon_a + \varepsilon} + \frac{\varepsilon_b - \varepsilon}{(\varepsilon_b + \varepsilon)e^{dq} - \varepsilon_b + \varepsilon} + 1} \tag{2.17}$$

If this expression is compared to that of a single homogenous layer of dielectric constant ε (obtained by putting $\varepsilon_a = \varepsilon_b = \varepsilon$ in the above) it is seen that for the two-interface system the role of the effective relative dielectric constant is played by

$$\varepsilon_{\text{eff}} = \varepsilon \left[\frac{\varepsilon_a - \varepsilon}{(\varepsilon_a + \varepsilon)e^{dq} - \varepsilon_a + \varepsilon} + \frac{\varepsilon_b - \varepsilon}{(\varepsilon_b + \varepsilon)e^{dq} - \varepsilon_b + \varepsilon} + 1\right] \tag{2.18}$$

which describes the screening in the thin layer as a function of the layer thickness d. The dependence on q describes the nonlocality of the screening in the layer. Taking this expression to first order in d one obtains

$$\varepsilon_{\text{eff}} \approx \frac{\varepsilon_a + \varepsilon_b}{2} + \left[\frac{\varepsilon}{2} - \frac{\varepsilon_a^2 + \varepsilon_b^2}{4\varepsilon}\right] qd \tag{2.19}$$

Thus, if an expression for the dielectric constant of the thin layer is known, the effective dielectric constant of the system can be found. If the thin layer is modelled as a homogenous layer the average dielectric constant can be calculated as [10]

$$\varepsilon = 1 + \frac{i\tilde{\sigma}}{d\varepsilon_0\omega} \tag{2.20}$$

where $\tilde{\sigma}$ is the complex 2D sheet conductivity. Inserting this expression in Eqn. 2.19 and taking d to zero one obtains

$$\varepsilon_{\text{eff}} \approx \frac{\varepsilon_a + \varepsilon_b}{2} + \frac{iq\tilde{\sigma}}{2\varepsilon_0\omega} \tag{2.21}$$

Thus, if an expression for the ω and q dependent complex sheet conductivity is known the ω and q dependent effective dielectric function for the thin layer can be calculated. If the average dielectric constant $\varepsilon_{\text{ave}} = (\varepsilon_a + \varepsilon_b)/2$ and the 2D sheet susceptibility $\chi_{\text{2D}} = iq\tilde{\sigma}/(2\varepsilon_0\omega)$ are introduced the effective dielectric constant can be written as

$$\varepsilon_{\text{eff}} = \varepsilon_{\text{ave}} + \chi_{\text{2D}} \tag{2.22}$$

Upon Fourier transforming back to real space the potential becomes

$$U(r) = \frac{1}{2\pi} \int \frac{e^{i\boldsymbol{q}\cdot\boldsymbol{r}}}{q\varepsilon_{\text{eff}}(0,q)} d^2q = \frac{1}{2\pi} \int\limits_0^\infty \int\limits_0^{2\pi} \frac{e^{iqr\cos\theta}}{q\varepsilon_{\text{eff}}(0,q)} qdqd\theta = \int\limits_0^\infty \frac{J_0(qr)}{\varepsilon_{\text{eff}}(0,q)} dq \tag{2.23}$$

where r is the distance between the two charges. The real space dielectric constant can be calculated by writing the potential as $U(r) = 1/\left[r\varepsilon(r)\right]$ so that

$$\varepsilon(r) = \frac{1}{rU(r)} \tag{2.24}$$

2.2 Calculation of conductivity

The real part of the q-dependent conductivity in units of the graphene DC-conductivity $\sigma_0 = e^2/(4\hbar)$ can be calculated from (App. A)

$$\text{Re}\left[\tilde{\sigma}(\omega, \boldsymbol{q})\right] = \frac{2\hbar\omega}{\pi q^2} \sum_c \sum_v \int \left|\langle\Psi_c, \boldsymbol{k} + \boldsymbol{q}|\, e^{i\boldsymbol{q}\cdot\boldsymbol{r}}\, |\Psi_v, \boldsymbol{k}\rangle\right|^2 \delta(E_{c,\boldsymbol{k}+\boldsymbol{q}} - E_{v,\boldsymbol{k}} - \hbar\omega) d^2k \tag{2.25}$$

where the sum over c and v ranges over all conduction bands and valence bands for which the transition energy $E_{c,\boldsymbol{k}+\boldsymbol{q}} - E_{v,\boldsymbol{k}}$ is equal to $\hbar\omega$ for some value of $\boldsymbol{k}$. The above formula describes the conductivity under indirect excitations from a valence band to a conduction band, i.e., excitations from a state $\boldsymbol{k}$ to $\boldsymbol{k} + \boldsymbol{q}$. This expression for the q-dependent conductivity transforms into the usual expression for the conductivity for small $\boldsymbol{q}$. This can be seen by expanding $e^{i\boldsymbol{q}\cdot\boldsymbol{r}} \approx 1 + i\boldsymbol{q}\cdot\boldsymbol{r}$ and using the fact that the two states are orthogonal. Thus, for small $\boldsymbol{q}$

$$\langle\Psi_c, \boldsymbol{k} + \boldsymbol{q}|\, e^{i\boldsymbol{q}\cdot\boldsymbol{r}}\, |\Psi_v, \boldsymbol{k}\rangle \approx \langle\Psi_c, \boldsymbol{k} + \boldsymbol{q}|\, 1 + i\boldsymbol{q}\cdot\boldsymbol{r}\, |\Psi_v, \boldsymbol{k}\rangle =$$
$$\langle\Psi_c, \boldsymbol{k} + \boldsymbol{q}|\Psi_v, \boldsymbol{k}\rangle + i\boldsymbol{q}\cdot\langle\Psi_c, \boldsymbol{k} + \boldsymbol{q}|\, \boldsymbol{r}\, |\Psi_v, \boldsymbol{k}\rangle \tag{2.26}$$

Since the two states are orthogonal the first term on the right hand side is identically zero. Thus, for small $\boldsymbol{q}$

$$\left|\langle\Psi_c,\boldsymbol{k}+\boldsymbol{q}|\,e^{i\boldsymbol{q}\cdot\boldsymbol{r}}\,|\Psi_v,\boldsymbol{k}\rangle\right|^2 \approx q^2\left|\langle\Psi_c,\boldsymbol{k}|\,\boldsymbol{r}\,|\Psi_v,\boldsymbol{k}\rangle\right|^2 \tag{2.27}$$

Using this expression in the q-dependent conductivity and rewriting the dipole matrix element into the momentum matrix element [2] the usual expression for the conductivity is obtained. Thus, the q-dependent conductivity has the usual conductivity as a limiting case. It should be noted that only with the Fourier transform convention chosen in App. A does the q-dependent conductivity correspond to the usual conductivity when $q \to 0$, thus, the convention chosen is particularly convenient in this case.

In the formalism of the tight binding method the matrix element between two states of the crystal is given by

$$\langle\Psi_c,\boldsymbol{k}+\boldsymbol{q}|\,e^{i\boldsymbol{q}\cdot\boldsymbol{r}}\,|\Psi_v,\boldsymbol{k}\rangle = \sum_p\sum_{p'} c_c^{p'}(\boldsymbol{k}+\boldsymbol{q})^* c_v^p(\boldsymbol{k})\,\langle\Phi^p,\boldsymbol{k}+\boldsymbol{q}|\,e^{i\boldsymbol{q}\cdot\boldsymbol{r}}\,|\Phi^{p'},\boldsymbol{k}\rangle \tag{2.28}$$

The matrix element between two Bloch states is

$$\langle\Phi^p,\boldsymbol{k}+\boldsymbol{q}|\,e^{i\boldsymbol{q}\cdot\boldsymbol{r}}\,|\Phi^{p'},\boldsymbol{k}\rangle = \sum_{lmn} e^{i(\boldsymbol{R}_{lmn}^p-\boldsymbol{R}_{000}^{p'})\cdot\boldsymbol{k}} e^{-i\cdot\boldsymbol{R}_{000}^{p'}\cdot\boldsymbol{q}}\,\langle\varphi^{p'},\boldsymbol{R}_{000}^{p'}|\,e^{i\boldsymbol{q}\cdot\boldsymbol{r}}\,|\varphi^p,\boldsymbol{R}_{lmn}^p\rangle \tag{2.29}$$

In principle there are two sums, one for each Bloch function, and a factor of $1/U$ (U being the number of unit cells), but due to the symmetry of the crystal one sum annihilates the factor of $1/U$. The matrix element between the atomic wave function $\varphi^{p'}$ at position $\boldsymbol{R}_{000}^{p'}$ and φ^p at position $\boldsymbol{R}_{lmn}^p$ can be calculated by assuming that the exponential factor $e^{i\boldsymbol{q}\cdot\boldsymbol{r}}$ does not vary substantially in the region of $\boldsymbol{r}$ for which the product φ^p and $\varphi^{p'}$ is different from zero. This is a reasonable assumption since the momentum transfer in optical processes is small and therefore $\boldsymbol{q}$ is small in magnitude. Under this assumption $\boldsymbol{r}$ in the exponential function can be replaced by $\boldsymbol{R}_{000}^{p'}$ and put outside the integral giving

$$\begin{aligned}\langle\Phi^p,\boldsymbol{k}+\boldsymbol{q}|\,e^{i\boldsymbol{q}\cdot\boldsymbol{r}}\,|\Phi^{p'},\boldsymbol{k}\rangle &\approx \sum_{lmn} e^{i(\boldsymbol{R}_{lmn}^p-\boldsymbol{R}_{000}^{p'})\cdot\boldsymbol{k}} e^{-i\cdot\boldsymbol{R}_{000}^{p'}\cdot\boldsymbol{q}} e^{i\cdot\boldsymbol{R}_{000}^{p'}\cdot\boldsymbol{q}}\,\langle\varphi^{p'},\boldsymbol{R}_{000}^{p'}|\varphi^p,\boldsymbol{R}_{lmn}^p\rangle \\ &= \sum_{lmn} e^{i(\boldsymbol{R}_{lmn}^p-\boldsymbol{R}_{000}^{p'})\cdot\boldsymbol{k}}\,\langle\varphi^{p'},\boldsymbol{R}_{000}^{p'}|\varphi^p,\boldsymbol{R}_{lmn}^p\rangle \\ &= S^{pp'}\end{aligned} \tag{2.30}$$

Using this result the matrix element between two states of the crystal becomes

$$\begin{aligned}\langle\Psi_c,\boldsymbol{k}+\boldsymbol{q}|\,e^{i\boldsymbol{q}\cdot\boldsymbol{r}}\,|\Psi_v,\boldsymbol{k}\rangle &= \sum_p\sum_{p'} c_{c,\boldsymbol{k}+\boldsymbol{q}}^{p'\,*} c_v^p(\boldsymbol{k}) S^{pp'} \\ &= \boldsymbol{c}_{c,\boldsymbol{k}+\boldsymbol{q}}^* \cdot \hat{\mathsf{S}} \cdot \boldsymbol{c}_{v,\boldsymbol{k}} \\ &\approx \boldsymbol{c}_{c,\boldsymbol{k}+\boldsymbol{q}}^* \cdot \boldsymbol{c}_{v,\boldsymbol{k}}\end{aligned} \tag{2.31}$$

where overlap has been neglected in the last step.

2.3 Gapped graphene

Using a slightly modified version of the simple two band model of graphene in order to describe graphene with a gap (see App. C for a description of the two band model) the conductivity can be estimated and used to calculate the dielectric function. This model will be referred to as the gapped two band model. The model makes no assumptions about the origin of the band gap and therefore the results apply to gapped graphene in general, at least within the validity of the approximations used in the model. In the two band model the tight binding Hamiltonian is given by (see App. B for information on tight binding)

$$\hat{\mathsf{H}}_{\mathrm{tb}} = \begin{pmatrix} 0 & -\gamma_1 f(\boldsymbol{k}) \\ -\gamma_1 f^*(\boldsymbol{k}) & 0 \end{pmatrix} \tag{2.32}$$

where the designation "tb" means "two band". This Hamiltonian is the simplest possible description of pure graphene. In order to describe graphene with a gap, the Hamiltonian is modified according to

$$\hat{\mathsf{H}}_{\mathrm{gtb}} = \begin{pmatrix} \alpha & -\gamma_1 f(\boldsymbol{k}) \\ -\gamma_1 f^*(\boldsymbol{k}) & -\alpha \end{pmatrix} \tag{2.33}$$

where "gtb" stands for "gapped two band". This Hamiltonian is the simplest possible description of gapped graphene. The eigenvalues of this Hamiltonian are found by solving the eigenvalue problem $\hat{\mathsf{H}}_{\mathrm{gtb}} \Psi_{j\boldsymbol{k}}(\boldsymbol{r}) = E \Psi_{j\boldsymbol{k}}(\boldsymbol{r})$ (the overlap matrix is approximated by the unit matrix). The eigenvalue problem is rewritten according to

$$(\hat{\mathsf{H}}_{\mathrm{gtb}} - \hat{\mathsf{I}} E) \Psi_{j\boldsymbol{k}}(\boldsymbol{r}) = 0 \tag{2.34}$$

which has solutions other than the trivial one ($\Psi_{j\boldsymbol{k}} = 0$) only if the determinant is equal to zero. Thus, the eigenvalues are determined by

$$\begin{vmatrix} \alpha - E & -\gamma_1 f(\boldsymbol{k}) \\ -\gamma_1 f^*(\boldsymbol{k}) & -\alpha - E \end{vmatrix} = 0 \tag{2.35}$$

The energy eigenvalues are found to be given by $E = \pm\sqrt{\alpha^2 + \gamma_1^2 |f(\boldsymbol{k})|^2}$, where the positive solution corresponds to the conduction band while the negative solution corresponds to the valence band. The gap is $E_g = 2\alpha$. The band gap remains in the K point since the expression for $f(\boldsymbol{k})$ is the same as in the two band model. By solving the eigenvalue problem the eigenvectors in a basis of sub lattice Bloch functions are found to be

$$|c, \boldsymbol{k}\rangle = \left(e^{i\theta_{\boldsymbol{k}}} \sqrt{(E_{c,\boldsymbol{k}} + \alpha)/(2E_{c,\boldsymbol{k}})}, \quad \sqrt{(E_{c,\boldsymbol{k}} - \alpha)/(2E_{c,\boldsymbol{k}})} \right) \tag{2.36}$$

$$|v, \boldsymbol{k}\rangle = \left(-e^{i\theta_{\boldsymbol{k}}} \sqrt{(E_{v,\boldsymbol{k}} + \alpha)/(2E_{v,\boldsymbol{k}})}, \quad \sqrt{(E_{v,\boldsymbol{k}} - \alpha)/(2E_{v,\boldsymbol{k}})} \right) \tag{2.37}$$

where $e^{i\theta_{\boldsymbol{k}}}$ is given by $f(\boldsymbol{k})/|f(\boldsymbol{k})|$. These eigenvectors have been obtained simply by solving the tight binding eigenvalue problem with the overlap matrix equal to the unit matrix, and demanding that the eigenvectors are orthonormal. To calculate the conductivity the matrix element of $e^{i\boldsymbol{q}\cdot\boldsymbol{r}}$ between the state of wave vector $\boldsymbol{k}$ in the valence band and the state of $\boldsymbol{k}+\boldsymbol{q}$ in the conduction band is needed. Using Eqn. 2.31 the matrix element is given simply by

$$
\langle\Psi_c,\boldsymbol{k}+\boldsymbol{q}|\,e^{i\boldsymbol{q}\cdot\boldsymbol{r}}\,|\Psi_v,\boldsymbol{k}\rangle \approx \langle c,\boldsymbol{k}+\boldsymbol{q}|v,\boldsymbol{k}\rangle =
$$
$$
= \frac{1}{2\sqrt{E_{c,\boldsymbol{k}+\boldsymbol{q}}\,|E_{v,\boldsymbol{k}}|}}\left[\sqrt{(E_{c,\boldsymbol{k}+\boldsymbol{q}}-\alpha)\,|E_{v,\boldsymbol{k}}-\alpha|} - e^{i(\theta_{\boldsymbol{k}}-\theta_{\boldsymbol{k}+\boldsymbol{q}})}\sqrt{(E_{c,\boldsymbol{k}+\boldsymbol{q}}+\alpha)\,|E_{v,\boldsymbol{k}}+\alpha|}\right]
$$
$$
(2.38)
$$

where the absolute values come from the fact that $E_{v,\boldsymbol{k}}-\alpha < 0$, $E_{v,\boldsymbol{k}}+\alpha \leq 0$ and $E_{v,\boldsymbol{k}} \leq 0 \ \forall \ \boldsymbol{k}$. Using the fact that $|a|^2 = a^2$ and $\sqrt{|a|^2} = -a$, $a \leq 0$ the squared matrix element becomes

$$
\left|\langle\Psi_c,\boldsymbol{k}+\boldsymbol{q}|\,e^{i\boldsymbol{q}\cdot\boldsymbol{r}}\,|\Psi_v,\boldsymbol{k}\rangle\right|^2 \approx \frac{1}{2}\left[1 + \frac{\alpha^2 + \gamma_1^2\,|f_{\boldsymbol{k}+\boldsymbol{q}}f_{\boldsymbol{k}}|\cos(\theta_{\boldsymbol{k}}-\theta_{\boldsymbol{k}+\boldsymbol{q}})}{E_{c,\boldsymbol{k}+\boldsymbol{q}}E_{v,\boldsymbol{k}}}\right] \qquad (2.39)
$$

where the approximate equality stems from Eqn. 2.31. The cosine can be calculated directly using Euler's formulas so that it is not necessary to calculate the angles. In fact, one gets

$$
|f_{\boldsymbol{k}}|\,|f_{\boldsymbol{k}+\boldsymbol{q}}|\cos(\theta_{\boldsymbol{k}}-\theta_{\boldsymbol{k}+\boldsymbol{q}}) = \frac{1}{2}\left(f_{\boldsymbol{k}}f_{\boldsymbol{k}+\boldsymbol{q}}^* + f_{\boldsymbol{k}+\boldsymbol{q}}f_{\boldsymbol{k}}^*\right) = \mathrm{Re}\,[f_{\boldsymbol{k}}]\,\mathrm{Re}\,[f_{\boldsymbol{k}+\boldsymbol{q}}] + \mathrm{Im}\,[f_{\boldsymbol{k}}]\,\mathrm{Im}\,[f_{\boldsymbol{k}+\boldsymbol{q}}]
$$
$$
(2.40)
$$

which is more suitable for numerical computations. With this expression for the matrix elements one can return to Eqn. 2.25 and calculate the conductivity.

Chapter 3

Wannier model of excitons

3.1 The Bethe-Salpeter equation

Excitons are, as the name suggests, a quasiparticle arising as a consequence of an excitation in an insulator or a semiconductor. In a semiconductor it is created when a photon is absorbed by an electron, raising the electron into a conduction band and leaving a "hole" in the valence band, i.e., a missing electron. The electron and the hole are free to move through the crystal. Since the electron is negatively charged and the hole acts as a positive charge the two particles are bound together much like the electron in a hydrogen atom is bound to the nucleus. This effectively reduces the energy of the exciton quasiparticle compared to the energy of a free electron and a free hole. The strength of the binding between the electron and the hole depends on the nature of the material in question, and effectively divides excitons into two categories [15]

1. Frenkel excitons: In a material of low screening the Coulomb attraction between the electron and the hole is strong and tends to localize the exciton, so that the electron and the hole are close together. The binding energy of a Frenkel exciton is on the order of 1 eV.

2. Wannier excitons: If the material has a high dielectric constant the Coulomb potential is strongly screened and the exciton binding energy is on the order of 0.1 eV. The Wannier exciton is delocalized and is "spread" out over several unit cells in the crystal.

In this chapter the Wannier model of excitonic effects in semiconductors will be derived. This model applies to Wannier excitons. The model is derived for 3D but it is easily adapted to 2D. In a crystal the many particle ground state is given by the following Slater determinant [16]

$$|0\rangle = |\overset{+}{v_1}\overset{-}{v_1}\overset{+}{v_2}\overset{-}{v_2}\dots\overset{+}{v_N}\overset{-}{v_N}| \tag{3.1}$$

where $+$ means a spin up single electron state, $-$ means a spin down single electron state, and v indicates a valence band state. This is the Hartree-Fock (HF) many-particle ground state. In the HF method the many-particle wave function is written as a single Slater determinant as the one given above. In order to go beyond the HF method the wave function is written

as a linear combination of multiple Slater determinants. One might then wonder how these determinants should be constructed since all valence states are already used in the HF single determinant wave function. The conduction band states have not been used however, and so one writes the wave function as a linear combination of the HF wave function and all singly excited determinant wave functions. In a singly excited state an electron is excited from some valence band state to a conduction band state. Since optical excitations do not flip spins, the spin is conserved in the excitation process. A singly excited state with the spin preserved can be constructed by making the substitution $\overset{+}{v_i} \to \overset{+}{c_j}$ or $\bar{v}_i \to \bar{c}_j$ in the ground state Slater determinant

$$|\overset{+}{v_i} \to \overset{+}{c_j}\rangle = |\ldots\ldots \overset{+}{c_j}\bar{v}_i \ldots\ldots| \tag{3.2}$$

$$|\bar{v}_i \to \bar{c}_j\rangle = |\ldots\ldots \overset{+}{v_i}\bar{c}_j \ldots\ldots| \tag{3.3}$$

None of these states have definite total spin. The linear combination

$$|v_i \to c_j\rangle = \frac{1}{\sqrt{2}}\left[|\overset{+}{v_i} \to \overset{+}{c_j}\rangle + |\bar{v}_i \to \bar{c}_j\rangle\right] \tag{3.4}$$

has definite total spin $S = 0$ and is thus a singlet state. Using the HF ground state as a starting point an excited state of the crystal is now written as the HF ground state wave function ($|0\rangle$) plus a linear combination of all possible singlet states

$$|\text{exc}\rangle = \Psi_0 |0\rangle + \sum_{ij} \Psi_{ij} |v_i \to c_j\rangle \tag{3.5}$$

in the following the HF ground state wave function will be absorbed in the summation above so that the excited wave function is written as

$$|\text{exc}\rangle = \sum_{ij} \Psi_{ij} |v_i \to c_j\rangle = \Psi_0 |0\rangle + \Psi_{11} |v_1 \to c_1\rangle + \Psi_{12} |v_1 \to c_2\rangle \ldots \tag{3.6}$$

where the summation now covers all the singlet states but also the HF ground state. The energy of this excited state is given by the expectation value of the Hamilton operator

$$\langle\text{exc}| \hat{H} |\text{exc}\rangle = E_{\text{exc}} \tag{3.7}$$

with the Hamilton operator given as

$$\hat{H} = \sum_{n=1}^{2N} \hat{h}_n + \frac{1}{2}\sum_{n=1}^{2N}\sum_{m=1}^{2N} V(\boldsymbol{r}_n - \boldsymbol{r}_m), \qquad V(\boldsymbol{r}_n - \boldsymbol{r}_m) = \frac{e^2}{4\pi\varepsilon_0 |\boldsymbol{r}_n - \boldsymbol{r}_m|} \tag{3.8}$$

Here $\hat{h}$ is the one electron terms, i.e., their kinetic energy and their interaction with the (stationary) nuclei. Thus, one needs to find matrix elements of the Hamiltonian between two singlet states

$$\hat{H}_{ij,kl} = \langle v_i \rightarrow c_j | \hat{H} | v_k \rightarrow c_l \rangle \tag{3.9}$$

and also between the ground state and singlet states

$$\hat{H}_{0,kl} = \langle 0 | \hat{H} | v_k \rightarrow c_l \rangle \tag{3.10}$$

It can be shown that the matrix element between the ground state and a singly excited state vanishes [17]. Using the definition of the singlet states Eqn. 3.4 the matrix elements are given by

$$\hat{H}_{ij,kl} = \frac{1}{2} \big[\langle v_i^+ \rightarrow c_j^+ | \hat{H} | v_k^+ \rightarrow c_l^+ \rangle + \langle v_i^+ \rightarrow c_j^+ | \hat{H} | \bar{v}_k \rightarrow \bar{c}_l \rangle +$$
$$\langle \bar{v}_i \rightarrow \bar{c}_j | \hat{H} | v_k^+ \rightarrow c_l^+ \rangle + \langle \bar{v}_i \rightarrow \bar{c}_j | \hat{H} | \bar{v}_k \rightarrow \bar{c}_l \rangle \big] \tag{3.11}$$

$\hat{F} = \sum\limits_{i=1}^{N} \hat{f}(x_i)$, a sum of one electron operators

   a. $F_{\Psi\Psi'} = 0$, if Ψ and Ψ' differ in two or more spin-orbitals.

   b. $F_{\Psi\Psi'} = \langle \psi_k | \hat{f} | \psi_k' \rangle$, if Ψ and Ψ' differ in only the k'th spin-orbitals.

   c. $F_{\Psi\Psi'} = \sum\limits_{k} \langle \psi_k | \hat{f} | \psi_k \rangle$, if $\Psi = \Psi'$, i.e. they do not differ in any spin-orbitals.

$$\tag{3.12}$$

$\hat{G} = \frac{1}{2} \sum\limits_{i=1}^{N} \sum\limits_{j=1}^{N} \hat{g}(x_i, x_j)$, a sum of two electron operators

   a. $G_{\Psi\Psi'} = 0$, if Ψ and Ψ' differ in three or more spin-orbitals.

   b. $G_{\Psi\Psi'} = \langle \psi_k \psi_l | \hat{g} | \psi_k' \psi_l' \rangle - \langle \psi_k \psi_l | \hat{g} | \psi_l' \psi_k' \rangle$, if Ψ and Ψ' differ in exactly two spin-orbitals.

   c. $G_{\Psi\Psi'} = \sum\limits_{k \neq l} [\langle \psi_k \psi_l | \hat{g} | \psi_k' \psi_l \rangle - \langle \psi_k \psi_l | \hat{g} | \psi_l \psi_k' \rangle]$, if Ψ and Ψ' differ in exactly one spin-orbital.

   d. $G_{\Psi\Psi'} = \frac{1}{2} \sum\limits_{k=1}^{N} \sum\limits_{l=1}^{N} [\langle \psi_k \psi_l | \hat{g} | \psi_k \psi_l \rangle - \langle \psi_k \psi_l | \hat{g} | \psi_l \psi_k \rangle]$, if $\Psi = \Psi'$, i.e. they do not differ in any spin-orbitals.

$$\tag{3.13}$$

The matrix elements between singly excited states (the states given by Eqn. 3.3) are found by using the rules for evaluating matrix elements between Slater determinants, see Eqn. 3.12 and Eqn. 3.13 (or [18] for more information). Since the Hamiltonian is spin independent, the first and fourth term as well as the second and the third term are equivalent, thus

$$\hat{\mathsf{H}}_{ij,kl} = \langle \overset{+}{v_i} \rightarrow \overset{+}{c_j} | \hat{H} | \overset{+}{v_k} \rightarrow \overset{+}{c_l} \rangle + \langle \overset{+}{v_i} \rightarrow \overset{+}{c_j} | \hat{H} | \overset{-}{v_k} \rightarrow \overset{-}{c_l} \rangle \tag{3.14}$$

For the off diagonal elements, i.e., for $i \neq k$ and $j \neq l$, the Slater determinants in both terms differ in exactly two spin-orbitals, namely the i'th and the k'th. Therefore, using rule (b) of Eqn. 3.13 one gets

$$\langle \overset{+}{v_i} \rightarrow \overset{+}{c_j} | \hat{H} | \overset{+}{v_k} \rightarrow \overset{+}{c_l} \rangle = \langle v_k c_j | V | c_l v_i \rangle - \langle v_k c_j | V | v_i c_l \rangle \tag{3.15}$$

$$\langle \overset{+}{v_i} \rightarrow \overset{+}{c_j} | \hat{H} | \overset{-}{v_k} \rightarrow \overset{-}{c_l} \rangle = \langle v_k c_j | V | c_l v_i \rangle \tag{3.16}$$

For the diagonal matrix elements, $i = k$ and $j = l$, and with the same argumentation as above, the cross term yields

$$\langle \overset{+}{v_i} \rightarrow \overset{+}{c_j} | \hat{H} | \overset{-}{v_i} \rightarrow \overset{-}{c_j} \rangle = \langle c_j v_i | V | v_i c_j \rangle \tag{3.17}$$

The calculation of the direct-term for the diagonal matrix is somewhat tedious. Using the rules for evaluating matrix elements of both one and two electron operators though, the calculation is fairly straightforward. Only the result is given here

$$\langle \overset{+}{v_i} \rightarrow \overset{+}{c_j} | \hat{H} | \overset{+}{v_i} \rightarrow \overset{+}{c_j} \rangle = \langle 0 | \hat{H} | 0 \rangle + E_{c_j} - E_{v_i} + \langle c_j v_i | V | v_i c_j \rangle - \langle c_j v_i | V | c_j v_i \rangle \tag{3.18}$$

where E_{c_j} and E_{v_i} are quasiparticle energies given by

$$E_{c_j} = \langle c_j | \hat{h} | c_j \rangle + \sum_{n=1}^{N} \{ 2 \langle v_n c_j | V | v_n c_j \rangle - \langle v_n c_j | V | c_j v_n \rangle \} \tag{3.19}$$

$$E_{v_i} = \langle v_i | \hat{h} | v_i \rangle + \sum_{n=1}^{N} \{ 2 \langle v_n v_i | V | v_n v_i \rangle - \langle v_n v_i | V | v_i v_n \rangle \} \tag{3.20}$$

The quasiparticle energies have quite simple physical interpretations. E_{c_j} represents the total energy of an electron in the j'th conduction band state. The first term represents its kinetic energy and its interaction with the nuclei of the lattice, while the summation represents its Coulomb and exchange interaction with the remaining electrons in the valence band. E_{v_i} has a similar interpretation but for an electron in the i'th valence band state.

With the above expression for the matrix elements between singly excited states the matrix element between any two singlets is given by

$$\hat{\mathsf{H}}_{ij,kl} = \left(E_{c_j} - E_{v_i} \right) \delta_{ik} \delta_{jl} + 2 \langle v_k c_j | V | c_l v_i \rangle - \langle v_k c_j | V | v_i c_l \rangle \tag{3.21}$$

where the energy is measured relative to the ground state energy $\langle 0 | \hat{H} | 0 \rangle$. The matrix equation to be solved is

$$\sum_{ij} H_{kl,ij}\Psi_{ij} = E_{\text{exc}}\Psi_{kl} \tag{3.22}$$

In a solid the individual states are indexed by the particular band they belong to and the momentum of the state. Thus, the indexes i, j, k, l are transformed according to $i \rightarrow v\boldsymbol{k}$, $j \rightarrow c\boldsymbol{k}$, $k \rightarrow v'\boldsymbol{k}'$ and $l \rightarrow c'\boldsymbol{k}'$. Only singly excited states between states of equal $\boldsymbol{k}$ are allowed, i.e., only excitations of the type $|v\boldsymbol{k} \rightarrow c\boldsymbol{k}\rangle$. This makes sense because photons carry negligible momentum. The matrix element then looks like (still measured relative to the ground state energy)

$$H_{vc\boldsymbol{k},v'c'\boldsymbol{k}'} = (E_{c\boldsymbol{k}} - E_{v\boldsymbol{k}})\,\delta_{cc'}\delta_{vv'}\delta_{\boldsymbol{k}\boldsymbol{k}'} + 2\,\langle cv\boldsymbol{k}|\,V_X\,|c'v'\boldsymbol{k}'\rangle - \langle cv\boldsymbol{k}|\,V_C\,|c'v'\boldsymbol{k}'\rangle \tag{3.23}$$

with the Coulomb and exchange matrix elements defined by

$$\langle cv\boldsymbol{k}|\,V_C\,|c'v'\boldsymbol{k}'\rangle = \frac{1}{\varepsilon}\iint \varphi^*_{c\boldsymbol{k}}(\boldsymbol{r})\varphi^*_{v'\boldsymbol{k}'}(\boldsymbol{r}')V(\boldsymbol{r}-\boldsymbol{r}')\varphi_{c'\boldsymbol{k}'}(\boldsymbol{r})\varphi_{v\boldsymbol{k}}(\boldsymbol{r}')d^3rd^3r' \tag{3.24}$$

$$\langle cv\boldsymbol{k}|\,V_X\,|c'v'\boldsymbol{k}'\rangle = \iint \varphi^*_{c\boldsymbol{k}}(\boldsymbol{r})\varphi^*_{v'\boldsymbol{k}'}(\boldsymbol{r}')V(\boldsymbol{r}-\boldsymbol{r}')\varphi_{v\boldsymbol{k}}(\boldsymbol{r})\varphi_{c'\boldsymbol{k}'}(\boldsymbol{r}')d^3rd^3r' \tag{3.25}$$

The screening $1/\varepsilon$ has been introduced since the Coulomb potential is screened by the surrounding charges. Using the transformations of i,j,k and l as it was done earlier, the matrix equation now looks like

$$\sum_{vc\boldsymbol{k}} H_{v'c'\boldsymbol{k}',vc\boldsymbol{k}}\Psi_{vc\boldsymbol{k}} = E_{\text{exc}}\Psi_{v'c'\boldsymbol{k}'} \tag{3.26}$$

This matrix equation, with the matrix element given by Eqn. 3.23 is the Bethe-Salpeter equation.

3.2 The Wannier model

In order to proceed the eigenstates of the crystal are written in accordance with the Bloch theorem as

$$\varphi_{\alpha\boldsymbol{k}}(\boldsymbol{r}) = \frac{1}{\sqrt{\Omega}}u_{\alpha\boldsymbol{k}}(\boldsymbol{r})e^{i\boldsymbol{k}\cdot\boldsymbol{r}} \tag{3.27}$$

where the functions $u_{\alpha\boldsymbol{k}}(\boldsymbol{r})$ are lattice periodic functions obeying

$$\frac{1}{\Omega_{\text{UC}}}\int\limits_{\text{UC}} |u_{\alpha\boldsymbol{k}}(\boldsymbol{r})|^2\,d^3r = 1 \tag{3.28}$$

where the integral is taken over one unit cell. This in turn ensures that the function Eqn. 3.27 is normalized. Inserting the expression Eqn. 3.27 for the crystal states into the Coulomb and exchange matrix element one gets, first for the Coulomb matrix element

$$
\begin{aligned}
\langle cv\boldsymbol{k}|\, V_C\, |c'v'\boldsymbol{k}'\rangle &= \frac{1}{\varepsilon\Omega^2} \iint u_{c\boldsymbol{k}}^*(\boldsymbol{r})e^{-i\boldsymbol{k}\cdot\boldsymbol{r}} u_{v'\boldsymbol{k}'}^*(\boldsymbol{r}')e^{-i\boldsymbol{k}'\cdot\boldsymbol{r}'} V(\boldsymbol{r}-\boldsymbol{r}') u_{c'\boldsymbol{k}'}(\boldsymbol{r})e^{i\boldsymbol{k}'\cdot\boldsymbol{r}} u_{v\boldsymbol{k}}(\boldsymbol{r}')e^{i\boldsymbol{k}\cdot\boldsymbol{r}} d^3r\, d^3r' \\
&= \frac{1}{\varepsilon\Omega^2} \iint u_{c\boldsymbol{k}}^*(\boldsymbol{r}) u_{c'\boldsymbol{k}'}(\boldsymbol{r}) e^{i(\boldsymbol{k}'-\boldsymbol{k})\cdot\boldsymbol{r}} u_{v\boldsymbol{k}}(\boldsymbol{r}') u_{v'\boldsymbol{k}'}^*(\boldsymbol{r}') e^{i(\boldsymbol{k}-\boldsymbol{k}')\cdot\boldsymbol{r}'} V(\boldsymbol{r}-\boldsymbol{r}') d^3r\, d^3r'
\end{aligned}
$$
(3.29)

Now, the functions $u_{\alpha\boldsymbol{k}}$ are rapidly varying lattice periodic functions while the functions $e^{i(\boldsymbol{k}-\boldsymbol{k}')\cdot\boldsymbol{r}}$ are slowly varying. . Thus, the product $u_{v\boldsymbol{k}}u_{v'\boldsymbol{k}'}^*$ is rapidly varying and the product $V(\boldsymbol{r}-\boldsymbol{r}')e^{i(\boldsymbol{k}-\boldsymbol{k}')\cdot\boldsymbol{r}}$ is slowly varying. This behaviour can be exploited in evaluating the integral. Let $S(\boldsymbol{r})$ be a slowly varying function and $R(\boldsymbol{r})$ be a rapidly varying lattice periodic function, then

$$
\int_{\Omega_{\text{UC}}} S(\boldsymbol{r})R(\boldsymbol{r})d^3r = \sum_{l=1}^{N} \int_{\Omega_{\text{UC}}(\boldsymbol{R}_l)} S(\boldsymbol{r})R(\boldsymbol{r})d^3r
$$
(3.30)

(3.31)

where the integral is taken over the unit cell with midpoint $\boldsymbol{R}_l$ and the contributions from every single unit cell are summed. This gives the same result as if the integral was taken over the entire crystal. Now, the slowly varying function is nearly constant across a single unit cell so that $S(\boldsymbol{r})$ can be replaced by its value at the midpoint of the unit cell

$$
\begin{aligned}
\int_{\Omega_{\text{UC}}} S(\boldsymbol{r})R(\boldsymbol{r})d^3r &\approx \sum_{l=1}^{N} S(\boldsymbol{R}_l) \int_{\Omega_{\text{UC}}(\boldsymbol{R}_l)} R(\boldsymbol{r})d^3r \\
&= \sum_{l=1}^{N} S(\boldsymbol{R}_l) \int_{\Omega_{\text{UC}}} R(\boldsymbol{r})d^3r
\end{aligned}
$$
(3.32)

The last equality follows since it does not matter over which unit cell the integration is performed because $R(\boldsymbol{r})$ is lattice periodic. Finally, since the slowly varying functions barely varies across a single unit cell one can multiply and divide the right hand side by Ω_{UC}, treat Ω_{UC} as a volume element and rewrite the summation into an integral over the entire crystal

$$
\int_{\Omega_{\text{UC}}} R(\boldsymbol{r})S(\boldsymbol{r})d^3r \approx \frac{1}{\Omega_{\text{UC}}} \int_{\Omega} S(\boldsymbol{r})d^3r \int_{\Omega_{\text{UC}}} R(\boldsymbol{r})d^3r
$$
(3.33)

Using this result first for $\boldsymbol{r}$ and then for $\boldsymbol{r}'$ the following is obtained for the Coulomb matrix element

$$\langle cv\boldsymbol{k}| V_C |c'v'\boldsymbol{k}'\rangle = \frac{1}{\varepsilon\Omega^2} I_{v'\boldsymbol{k}',v\boldsymbol{k}} I_{c\boldsymbol{k},c'\boldsymbol{k}'} \iint e^{i(\boldsymbol{k}-\boldsymbol{k}')\cdot(\boldsymbol{r}'-\boldsymbol{r})} V(\boldsymbol{r}-\boldsymbol{r}')d^3r\,d^3r' \tag{3.34}$$

$$I_{c\boldsymbol{k},c'\boldsymbol{k}'} = \frac{1}{\Omega_{\mathrm{UC}}} \int u_{c\boldsymbol{k}}^*(\boldsymbol{r}) u_{c'\boldsymbol{k}}(\boldsymbol{r}) d^3r \tag{3.35}$$

Since the integrand in Eqn. 3.34 only depends on the difference between $\boldsymbol{r}$ and $\boldsymbol{r}'$ one can rewrite the integral as

$$\langle cv\boldsymbol{k}| V_C |c'v'\boldsymbol{k}'\rangle = \frac{1}{\varepsilon\Omega} I_{v\boldsymbol{k},v'\boldsymbol{k}'} I_{c\boldsymbol{k},c'\boldsymbol{k}'} \int V(\boldsymbol{r}) e^{i(\boldsymbol{k}'-\boldsymbol{k})\cdot\boldsymbol{r}} d^3r \tag{3.36}$$

With the same argumentation as for the Coulomb matrix element, the exchange matrix element becomes

$$\langle cv\boldsymbol{k}| V_X |c'v'\boldsymbol{k}'\rangle = \frac{1}{\Omega^2} \iint u_{c\boldsymbol{k}}^*(\boldsymbol{r}) u_{v\boldsymbol{k}}(\boldsymbol{r}) u_{c'\boldsymbol{k}'}(\boldsymbol{r}') u_{v'\boldsymbol{k}'}(\boldsymbol{r}') V(\boldsymbol{r}-\boldsymbol{r}') d^3r\,d^3r'$$
$$= \frac{1}{\Omega} I_{c\boldsymbol{k},v\boldsymbol{k}} I_{v'\boldsymbol{k}',c'\boldsymbol{k}'} \int V(\boldsymbol{r}) d^3r \tag{3.37}$$

Where it is assumed that $V(\boldsymbol{r}-\boldsymbol{r}')$ is slowly varying over a single unit cell. Since the lattice periodic functions $u_{\alpha\boldsymbol{k}}(\boldsymbol{r})$ are orthogonal, one has for $\boldsymbol{k}=\boldsymbol{k}'$, $I_{\alpha\boldsymbol{k},\beta\boldsymbol{k}} = \delta_{\alpha\beta}$. If the $\boldsymbol{k}$ dependence of the lattice periodic functions is not too strong, one can assume that this relationship holds even when $\boldsymbol{k}\neq\boldsymbol{k}'$, i.e., $I_{\alpha\boldsymbol{k},\beta\boldsymbol{k}'} = \delta_{\alpha\beta}$. The matrix elements then become

$$\langle cv\boldsymbol{k}| V_C |c'v'\boldsymbol{k}'\rangle \approx \frac{1}{\varepsilon\Omega} \int V(\boldsymbol{r}) e^{i(\boldsymbol{k}'-\boldsymbol{k})\cdot\boldsymbol{r}} d^3r\,\delta_{vv'}\delta_{cc'} \tag{3.38}$$

$$\langle cv\boldsymbol{k}| V_X |c'v'\boldsymbol{k}'\rangle = 0 \tag{3.39}$$

From Eqn. 3.23 one finds the Hamiltonian matrix elements as

$$H_{vc\boldsymbol{k},v'c'\boldsymbol{k}'} = H_{vc\boldsymbol{k}\boldsymbol{k}'}\delta_{vv'}\delta_{cc'} = \left[(E_{c\boldsymbol{k}} - E_{v\boldsymbol{k}})\,\delta_{\boldsymbol{k}\boldsymbol{k}'} - \frac{1}{\varepsilon\Omega} \int V(\boldsymbol{r}) e^{i(\boldsymbol{k}'-\boldsymbol{k})\cdot\boldsymbol{r}} d^3r \right] \delta_{vv'}\delta_{cc'} \tag{3.40}$$

With this matrix element the matrix equation Eqn. 3.26 becomes

$$\sum_{\boldsymbol{k}} H_{vc\boldsymbol{k}\boldsymbol{k}'}\Psi_{vc\boldsymbol{k}} = E_{\mathrm{exc}}\Psi_{vc\boldsymbol{k}'} \tag{3.41}$$

since all matrix elements with $v\neq v'$ or $c\neq c'$ vanish. Inserting the matrix element Eqn. 3.40 into the above equation one obtains

$$(E_{c\boldsymbol{k}} - E_{v\boldsymbol{k}})\,\Psi_{vc\boldsymbol{k}} - \frac{1}{\varepsilon(2\pi)^3} \int \left[\int V(\boldsymbol{r}) e^{i(\boldsymbol{k}'-\boldsymbol{k})\cdot\boldsymbol{r}} d^3r \right] \Psi_{vc\boldsymbol{k}'} d^3k' = E_{\mathrm{exc}}\Psi_{vc\boldsymbol{k}} \tag{3.42}$$

where the $\boldsymbol{k}$ summation has been rewritten into an integral.

3.3   The effective mass approximation

The last approximation in the Wannier model consists in applying the effective mass approximation. In this approximation the bands are assumed to be approximately parabolic near the band gap in the Brillouin zone. The band energies $E_{c\boldsymbol{k}}$ and $E_{v\boldsymbol{k}}$ are accordingly written as

$$E_{c\boldsymbol{k}} = E_g + \frac{\hbar^2\boldsymbol{k}^2}{2m_e} \qquad E_{v\boldsymbol{k}} = -\frac{\hbar^2\boldsymbol{k}^2}{2m_h} \tag{3.43}$$

$$E_{c\boldsymbol{k}} - E_{v\boldsymbol{k}} = E_g + \frac{\hbar^2 k^2}{2m_{eh}} \tag{3.44}$$

where $m_{eh} = m_e m_h/(m_e + m_h)$ is the reduced effective mass. In the Coulomb term in Eqn. 3.42 the bracketed term is recognized as the Fourier transform of the potential $V(\boldsymbol{r})$ so that

$$\int V(\boldsymbol{r}) e^{i(\boldsymbol{k}'-\boldsymbol{k})\cdot\boldsymbol{r}} d^3r = V_{\boldsymbol{k}-\boldsymbol{k}'} \tag{3.45}$$

Using this result and the effective mass approximation one obtains

$$E_g \Psi_{\boldsymbol{k}} + \frac{\hbar^2 k^2}{2m_{eh}} \Psi_{\boldsymbol{k}} - \frac{1}{\varepsilon(2\pi)^3} \int V_{\boldsymbol{k}-\boldsymbol{k}'} \Psi_{\boldsymbol{k}'} d^3k' = E_{\text{exc}}\Psi_{\boldsymbol{k}} \tag{3.46}$$

The Coulomb term is the convolution of the potential and the wave function. From Fourier analysis it is known that the Fourier transform of a convolution is equal to the product of the Fourier components. Taking the Fourier transform of the above equation and using the relations

$$\frac{1}{(2\pi)^3} \int \Psi_{\boldsymbol{k}} e^{i\boldsymbol{k}\cdot\boldsymbol{r}} d^3k = \Psi(\boldsymbol{r}), \qquad \frac{1}{(2\pi)^3} \int \Psi_{\boldsymbol{k}} k^2 e^{i\boldsymbol{k}\cdot\boldsymbol{r}} d^3k = -\boldsymbol{\nabla}^2\Psi(\boldsymbol{r}) \tag{3.47}$$

one obtains the Wannier equation

$$\left[E_g - \frac{\hbar^2\boldsymbol{\nabla}^2}{2m_{eh}} \right] \Psi_{\text{exc}}(\boldsymbol{r}) - \frac{1}{\varepsilon(\boldsymbol{r})} V(\boldsymbol{r})\Psi_{\text{exc}}(\boldsymbol{r}) = E_{\text{exc}}\Psi_{\text{exc}}(\boldsymbol{r}) \tag{3.48}$$

The Wannier equation can be rewritten into more appropriate units by measuring length in terms of the effective unscreened Bohr radius $a_B^* = 4\pi\varepsilon_0\hbar^2/(m_{eh}e^2)$ and energy in terms of the effective unscreened Rydberg $\text{Ry}^* = \hbar^2/(2m_{eh}a_B^2)$. Using the expression Eqn. 3.8 for the potential the Wannier equation in natural exciton units becomes

$$\left[E_g - \nabla^2 \right] \Psi_{\text{exc}}(\boldsymbol{r}) - \frac{2}{r\varepsilon(r)}\Psi_{\text{exc}}(\boldsymbol{r}) = E_{\text{exc}}\Psi_{\text{exc}}(\boldsymbol{r}) \tag{3.49}$$

The binding energy of the exciton is given by $E_B = E_{\text{exc}} - E_g$ and in terms of the binding energy the above equation is

$$-\nabla^2 \Psi_{\text{exc}}(\boldsymbol{r}) - \frac{2}{r\varepsilon(r)}\Psi_{\text{exc}}(\boldsymbol{r}) = E_B \Psi_{\text{exc}}(\boldsymbol{r}) \tag{3.50}$$

Where the binding energy E_B is a negative quantity for the bound state solutions.

3.4 Linear bands

The effective mass approximation which was used above assumes that the bands are parabolic near the band gap. This is far from always the case and in gapped graphene for instance the bands are only parabolic very close to the band gap, but linear farther away. Thus, in gapped graphene a more accurate approximation for the bands near the band gap is

$$E_{c\boldsymbol{k}} = \sqrt{\alpha^2 + \gamma_c^2 k^2} \tag{3.51}$$

$$E_{v\boldsymbol{k}} = -\sqrt{\alpha^2 + \gamma_v^2 k^2} \tag{3.52}$$

where $E_g = 2\alpha$. These expressions reproduce the correct band structure near the band gap and are thus valid for low energy excitations. The goal here is to describe excitonic effects below the band gap, i.e., the excitonic energy states which are introduced below the lowest conduction band. Such excitations are low energy excitations and therefore the above expressions are good approximations for their purposes. For the two expressions to yield the correct effective masses for the present structures it is required that

$$\hbar^2 \left(\frac{d^2 E_{c\boldsymbol{k}}}{dk^2}\right)^{-1}\bigg|_{k=0} = m_e^* \tag{3.53}$$

and similarly for the valence band. Differentiating and taking the limit where $k \to 0$ one gets $\gamma_c^2 = \hbar^2 \alpha / m_e^*$ and thus

$$E_{c\boldsymbol{k}} = \sqrt{\alpha^2 + \alpha\hbar^2 k^2/m_e^*} \tag{3.54}$$

$$E_{v\boldsymbol{k}} = -\sqrt{\alpha^2 + \alpha\hbar^2 k^2/m_h^*} \tag{3.55}$$

If the gap is very small, i.e., for $\alpha \to 0$, these expressions describe pure graphene and should accordingly reproduce the correct Fermi velocity for k far away from the band gap. The Fermi velocity is equal to the slope of the bands divided by $\hbar$ and one finds for the conduction band and for $k \to \infty$, $v_F = \sqrt{\alpha/m_e^*}$. Using the values $m_e^* = 0.008 m_0$ (m_0 being the free electron mass) and $\alpha = 40.5\,\text{meV}$ ([1] or Tbl. 4.1) one obtains a Fermi velocity of $v_F \approx 0.94 * 10^6\,\text{m/s}$, close to the pure graphene value of $10^6\,\text{m/s}$.

Using these expressions for the band energies the eigenvalue problem Eqn. 3.42 becomes

$$\sqrt{\alpha^2 + \gamma_c^2 k^2}\Psi_{vc\boldsymbol{k}} + \sqrt{\alpha^2 + \gamma_v^2 k^2}\Psi_{vc\boldsymbol{k}} - \frac{1}{\varepsilon(2\pi)^3}\int V_{\boldsymbol{k}-\boldsymbol{k}'}\Psi_{vc\boldsymbol{k}}d^3k' = E_{\text{exc}}\Psi_{vc\boldsymbol{k}} \tag{3.56}$$

Now, this equation cannot be inversely Fourier transformed in a simple way as it was done under the effective mass approximation above. Instead, one has to calculate the kinetic energy terms (the two first terms on the left hand side) in $\boldsymbol{k}$-space. The Coulomb term (the third term on the left hand side) can still be inversely Fourier transformed in the same fashion as before. Thus, each term is evaluated in the most appropriate space by using the fact that the Fourier transform is a unitary transformation so that it preserves the inner product (App. D).

Chapter 4

Implementation and results

4.1 Screening in gapped graphene - two band model

In this section the q dependent conductivity spectra obtained using the two band model of gapped graphene are presented. The spectra are calculated using Eqn. 2.25 and the matrix element given by Eqn. 2.39. Due to the symmetry of the Brillouin zone the k integral in Eqn. 2.25 need in principle only be over the irreducible slice of the Brillouin zone, since the irreducible zone contains all the information contained in the whole Brillouin zone. One has to be aware however, of the asymmetry of the involved quantities, i.e., the matrix element and the transition energies. Due to the addition of the vector q to k of the final state the symmetry is broken and the result will depend on the choice of irreducible zone used for the integration. This is of course not physical since the result must not depend on how the integration is done, and should for all irreducible zones give the same result as if the integration was performed over the whole Brillouin zone. To restore the symmetry the integral is averaged over several q vectors of constant magnitude but with angles varying between 0 and 2π.
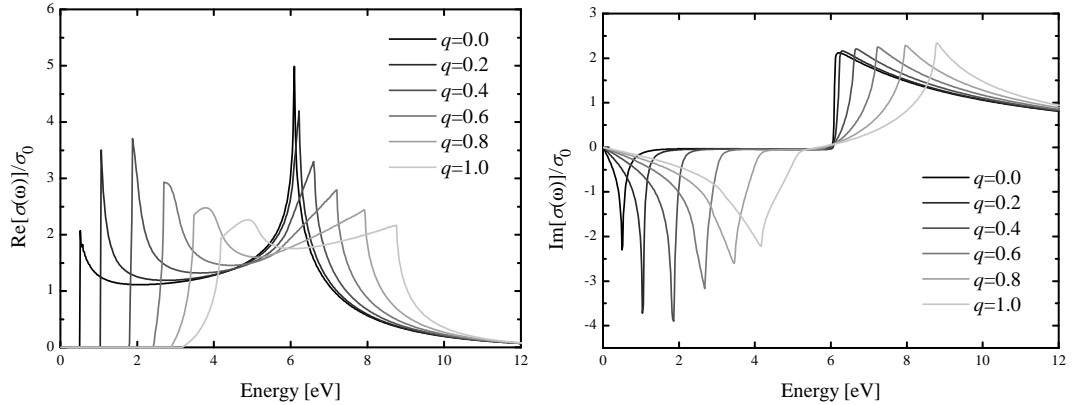

Figure 4.1: Real part (left) and imaginary part (right) of the graphene conductivity for various values of q as a function of energy. The band gap is set to 0.5 eV.

In order to evaluate the effective dielectric function given by Eqn. 2.21 the complex sheet conductivity is needed. The imaginary part of the conductivity can be calculated by using the

Kramers-Kronig relations which state that

$$R_i(\omega) = -\frac{2\omega}{\pi}\text{PV}\int\limits_0^\infty \frac{R_r(\omega')}{\omega'^2 - \omega^2}d\omega' \tag{4.1}$$

$$R_r(\omega) = \frac{2}{\pi}\text{PV}\int\limits_0^\infty \frac{\omega' R_i(\omega')}{\omega'^2 - \omega^2}d\omega' \tag{4.2}$$

where $\tilde{R}(\omega) = R_r(\omega) + iR_i(\omega)$ is an analytic function and PV means that the principal value of the integral has to be taken, which in practice means that the singularity is excluded from the integral. The numerical approximation to the imaginary part then becomes

$$R_i(\omega) = -\frac{2\omega}{\pi}\sum_{i\backslash i:\omega_i=\omega} \frac{R_r(\omega_i)}{\omega_i^2 - \omega^2}\Delta\omega \tag{4.3}$$

so that the summation includes all i except the one which leads to $\omega_i = \omega$. In Fig. 4.1 the real and imaginary part of the conductivity is plotted. 96 $\boldsymbol{q}$ vectors in the directions 0 to 2π are used, and the band gap is set to 0.5 eV. The k integration has been performed using the triangle integration method [10] with 4096 triangles. From the imaginary part of the conductivity one can proceed and calculate the effective dielectric function from Eqn. 2.21 for the 2D case and from Eqn. 2.18 for finite thicknesses of the graphene layer.
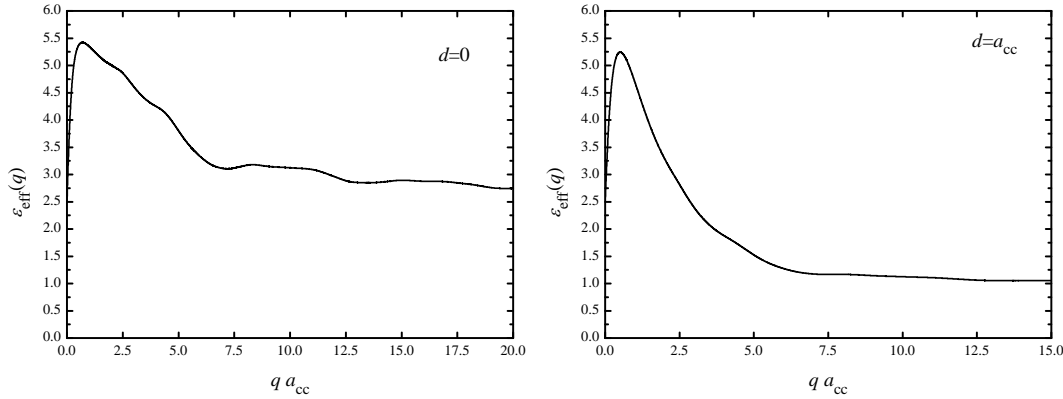

Figure 4.2: The effective dielectric function for two thicknesses of the graphene sheet calculated using a band gap of 0.5 eV.

In Fig. 4.2 the effective dielectric function, ε_{eff}, is plotted for two values of the thin layer thickness with $\varepsilon_a = \varepsilon_{\text{air}} = 1$ and $\varepsilon_b = \varepsilon_{\text{SiO}_2} = 4$, the 2D limit $d = 0$ and a finite thickness $d = a_{cc}$, with $a_{cc} = 1.42\text{Å}$ being the graphene carbon-carbon distance. It is seen that ε_{eff} converges to a constant value for large values of q. For the 2D limit ($d = 0$) the effective dielectric function starts in 2.5 for small q and converges to 2.5 for large q values. This makes sense intuitively since large q values correspond to small distances between the charges. Thus, when the charges are near each other or far apart the screening from the surrounding media dominates. For finite thicknesses the screening for large q approaches 1, i.e., the screening

in vacuum. One can say that the space between the two charges becomes depleted of other charges due to the repulsion as the charges get close together, and only the vacuum screening persists.

To calculate the real space dielectric function Eqn. 2.24 is used. The potential $U(r)$ is needed and can be calculated from Eqn. 2.23 by exploiting the behaviour of ε_{eff} for large q. For finite d the effective dielectric function ε_{eff} approaches 1 for large q and in the 2D limit it approaches the mean dielectric constant $\varepsilon_{\text{ave}} = (\varepsilon_a + \varepsilon_b)/2$. This means that the integral in Eqn. 2.23 can be evaluated in the following way

$$\int_0^\infty \frac{J_0(qr)}{\varepsilon_{\text{eff}}(0,q)} dq = \int_0^\infty \frac{J_0(qr)}{(\varepsilon_{\text{eff}} - a) + a} dq = \int_0^b \frac{J_0(qr)}{(\varepsilon_{\text{eff}} - a) + a} dq + \int_b^\infty \frac{J_0(qr)}{(\varepsilon_{\text{eff}} - a) + a} dq \qquad (4.4)$$

Here b is the value of q for which ε_{eff} reaches its asymptotic value a. For example, for the right figure in Fig. 4.2 $a = 1$ and $b \approx 12.5$. Thus, from b to ∞, $\varepsilon_{\text{eff}} - a = 0$ and therefore

$$\int_0^b \frac{J_0(qr)}{(\varepsilon_{\text{eff}} - a) + a} dq + \int_b^\infty \frac{J_0(qr)}{(\varepsilon_{\text{eff}} - a) + a} dq = \int_0^b \frac{J_0(qr)}{(\varepsilon_{\text{eff}} - a) + a} dq + \frac{1}{a} \int_b^\infty J_0(qr) dq =$$

$$\frac{1}{ar} + \int_0^b \left(\frac{J_0(qr)}{\varepsilon_{\text{eff}}} - \frac{J_0(qr)}{a} \right) dq = \frac{1}{ar} + \int_0^b \frac{a J_0(qr) - \varepsilon_{\text{eff}} J_0(qr)}{a\, \varepsilon_{\text{eff}}} dq \quad (4.5)$$

in the second step the lower limit in the last integral was changed from b to 0 and this was compensated for by subtracting $\frac{1}{a} \int_0^b J_0(qr) dq$. The integral from 0 to b can be easily evaluated numerically and in the actual calculations a trapezoidal numerical integration has been applied.

In Fig. 4.3 the real space dielectric function has been plotted for a number of graphene layer thicknesses. In the calculations the effective dielectric function has been calculated for 30000 values of q in the interval 0 to $80/a_{cc}$ using a band gap of 0.5 eV. The triangle integration has been performed using 361 triangles (210 k-points). Even though 361 triangles are not enough to obtain smooth conductivity spectra it is enough to obtain convergence in the final result for the dielectric function. The most important observation to be made from the calculation of the real space dielectric function, is that the final results are highly dependent on the thickness of the graphene layer, especially around $r \approx a_{cc}$. The actual thickness of a single graphene layer is poorly defined, and so it becomes difficult to obtain physically justified results for the screening in graphene on a substrate. From these results however, one can learn that the screening in graphene on a substrate is not so simple and cannot be determined simply from the properties of the surrounding media.

4.2 Exciton energies

Parabolic bands - the effective mass approximation

Using the real space dielectric function calculated above one can proceed and calculate the excitonic binding energies from the Wannier equation Eqn. 3.50 under the effective mass ap-
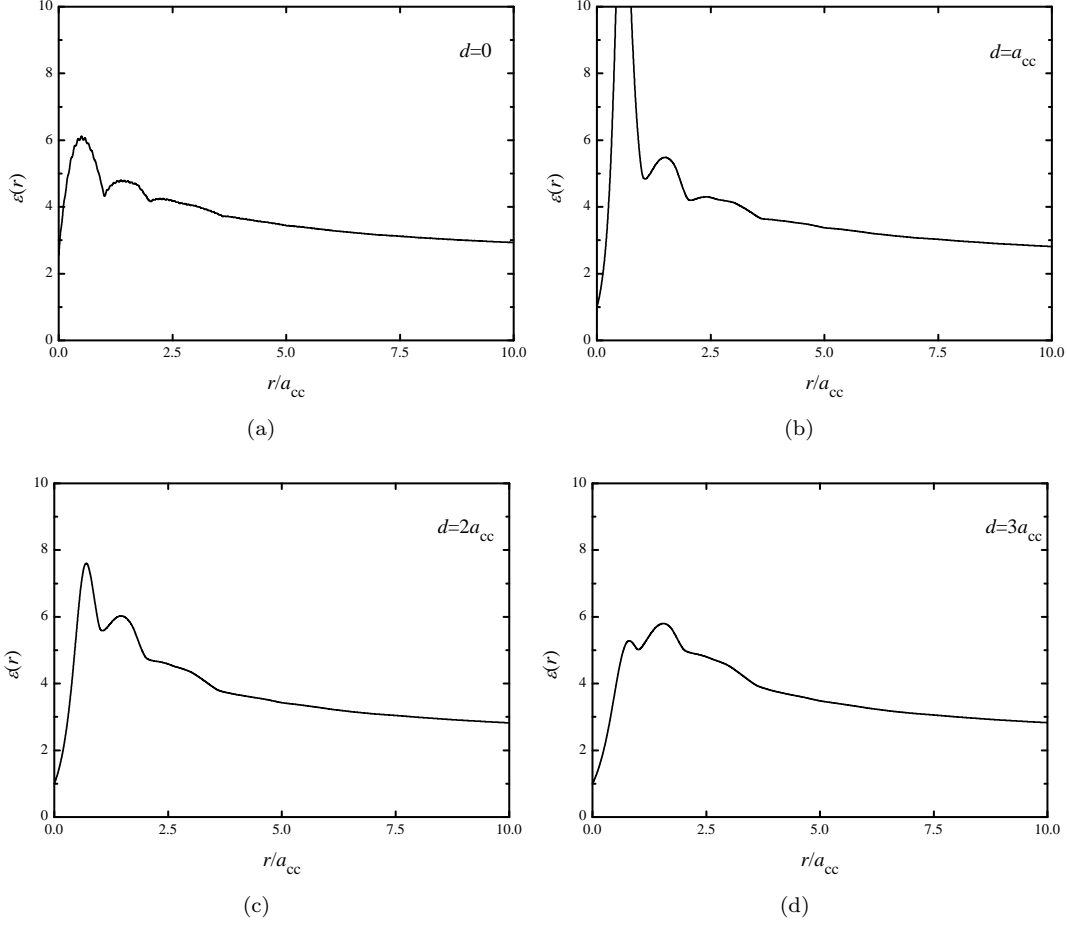
Figure 4.3: The real space dielectric function for four thicknesses of the graphene sheet calculated using a band gap size of 0.5 eV.

proximation. To determine the energies the exciton eigenstates are needed. Using a variational approach, one can assume that the radial part of the excitonic $1s$ state is given by

$$\Psi_{\text{exc}}(r) = 2\eta e^{-\eta r} \tag{4.6}$$

where η is a variational parameter to be determined later. The states are labeled similarly to those of the hydrogen atom since the Wannier equation is mathematically similar to the equation for the hydrogen atom, and thus has the same set of solutions. Inserting this expression into the 2D radial Wannier equation

$$\left[-\frac{d^2}{dr^2} - \frac{1}{r}\frac{d}{dr} - \frac{2}{r\varepsilon(r)} \right] \Psi_{\text{exc}}(r) = E_B \Psi_{\text{exc}}(r) \tag{4.7}$$

one obtains the following

$$\left[-\eta^2 + \frac{\eta}{r} - \frac{2}{r\varepsilon(r)}\right]\Psi_{\text{exc}}(r) = E_B\Psi_{\text{exc}}(r) \tag{4.8}$$

Left multiplication by $\Psi_{\text{exc}}^*(r)$ and subsequent integration over all space gives for the energy expectation value

$$E_B = \eta^2\left[1 - 8\int_0^\infty \frac{e^{-2\eta r}}{\varepsilon(r)}dr\right] \tag{4.9}$$

In order to determine the parameter η the above expression is differentiated and put equal to zero, thus

$$\frac{dE_B}{d\eta} = 2\eta\left[1 - 8\int_0^\infty \frac{e^{-2\eta r}}{\varepsilon(r)}dr + 8\eta\int_0^\infty \frac{re^{-2\eta r}}{\varepsilon(r)}dr\right] = 0 \tag{4.10}$$

Since no analytical expression for $\varepsilon(r)$ exists in the present model the integration has to be performed numerically. One can take advantage of the limiting behaviour of $\varepsilon(r)$ for large values of r, i.e., $\varepsilon(r)$ approaches ε_{ave} for large r, just as it was done above for numerical integration of expressions involving ε_{eff}. Upon doing this, the following expression is obtained

$$\frac{dE_B}{d\eta} = \frac{8b\eta - 4}{\varepsilon_{\text{ave}}}e^{-2\eta b} + 2\eta\left[1 - 8\int_0^b \frac{e^{-2\eta r}}{\varepsilon(r)}dr + 8\eta\int_0^b \frac{re^{-2\eta r}}{\varepsilon(r)}dr\right] = 0 \tag{4.11}$$

where b is the approximate value of r for which $\varepsilon(r)$ has converged to ε_{ave}. The above equation is solved numerically using the algorithm described in Alg. 4.1.

When the optimal value of η has been found, the energy can be calculated by inserting η into Eqn. 4.9. One has to remember that the energy calculated from this equation comes out in units of the effective unscreened Rydberg, $\text{Ry}^* = 13.6\,[\text{eV}]\cdot\mu$ where μ is the reduced effective excitonic mass $\mu = m_e m_h/(m_e + m_h)$ measured in units of the free electron mass m_0. The effective masses are taken from a quasi-particle (QP) tight binding model of graphene antidot lattices [1] [2]. It is important to remember that the thickness of the graphene layer, d, has to be measured in effective Bohr radii since d is coupled to q through Eqn. 2.18 and q is coupled to r through Eqn. 2.24 and Eqn. 2.23. The effective Bohr radius is given by $a_B = 0.529[\text{Å}]/\mu$.

In Fig. 4.4 the exciton binding energy is plotted as a function of layer thickness. The parameters used to make this plot are taken from the table in [2] calculated in the QP-TB model. They are given in Tbl. 4.1

In the figure it is seen that the excitonic binding energy does not vary much as a function of the layer thickness. That this makes good sense physically can be argued for by realizing that the Wannier exciton is very delocalized with the electron and the hole separated by several graphene lattice constants ($\approx 25\text{Å}$). The real space dielectric constant does not vary significantly as a function of layer thickness in this domain. The heavy dependence on the

---

Algorithm 1 Procedure for determining optimal value of η

```
 1: procedure NUMERICALSOLVER
 2:     Accuracy = 0.000001;
 3:     Direction = 0;
 4:     ThisVal = 0.0;
 5:     LastVal = 0.0;
 6:     Step = 10.0;
 7:     CurrEta=0.000001;                          ▷ A value close to but larger than zero
 8:     while Step > Accuracy do
 9:         ThisVal=dE_B/dN(CurrEta)     ▷ Calc. dE_B/dN in point CurrEta from Eqn. 4.11
10:         if Direction ≠ 0 then
11:             if ThisVal*LastVal < 0 then                       ▷ Check for sign reversal
12:                 Direction = -Direction;
13:                 Step=Step/2.0;
14:             end if
15:         else
16:             Direction = 1;                  ▷ Here it is assumed that the sought η is positive
17:         end if
18:         CurrEta = CurrEta + Direction*Step;
19:         LastVal = ThisVal;
20:     end while
21: end procedure
```

	$E_g = 81$	$E_g = 250$	$E_g = 358$	$E_g = 569$	$E_g = 577$	$E_g = 409$
m_e	0.008	0.033	0.053	0.097	0.232	0.349
m_h	0.008	0.031	0.047	0.083	0.658	0.130
μ	0.004	0.016	0.025	0.045	0.171	0.095

Table 4.1: Values of the effective masses and reduced effective masses used in calculating the exciton binding energies. The gap energies are in meV and the masses are in units of the free electron mass. The parameters are calculated from antidot lattices {12,1}, {12,3}, {10,3}, {8,3}, {10,5} and {10,7} (left to right in the table).

layer thickness is found at small distances on the order of a few graphene lattice constants. That the binding energy does not depend much on the layer thickness is convenient because it is difficult to argue physically for the actual thickness of the graphene layer. Due to the weak dependence the actual value of the thickness is not so important and choosing the graphene lattice constant as the thickness, the binding energies are as follows

$$E_{B,81} = -13\,\text{meV} \qquad E_{B,250} = -49\,\text{meV} \qquad E_{B,358} = -78\,\text{meV} \qquad E_{B,569} = -145\,\text{meV}$$
$$E_{B,577} = -316\,\text{meV} \qquad E_{B,409} = -593\,\text{meV}$$

For comparison, the binding energies calculated using Eqn. 1.1 by assuming that the graphene layer itself does not contribute to the screening, so that the screening is determined solely by the surrounding media, are given by
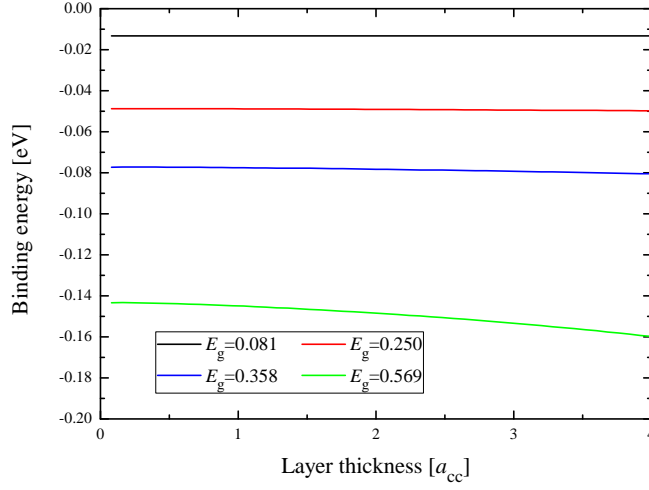
Figure 4.4: Exciton binding energies as a function of the layer thickness for a number of band gaps.

$$E_{B,81}^{\varepsilon=2.5} = -34\,\text{meV} \qquad E_{B,250}^{\varepsilon=2.5} = -139\,\text{meV} \qquad E_{B,358}^{\varepsilon=2.5} = -217\,\text{meV} \qquad E_{B,569}^{\varepsilon=2.5} = -391\,\text{meV}$$

$$E_{B,577}^{\varepsilon=2.5} = -820\,\text{meV} \qquad E_{B,409}^{\varepsilon=2.5} = -1484\,\text{meV}$$

Where the subscript $\varepsilon = 2.5$ is meant to indicate that these values of the binding energies are calculated using the simple estimate of the screening. Thus, the improved model of the screening reduces the binding energy by about a factor of 2.6. The binding energies in the simple model indicate that the model yield unphysical results for both the structure with $E_g = 577\,\text{meV}$ and the structure with $E_g = 409\,\text{meV}$, since the binding energy is larger than the band gap. In the more advanced model allowing for spatially varying screening the discrepancy is resolved for the structure with $E_g = 577\,\text{meV}$ while it persists for the $E_g = 409\,\text{meV}$ structure. Thus, the discrepancies are not resolved for all structures. It does seem however, that it is only the structures with large holes compared to the unit cell size which yield unphysical results.

Linear bands

The excitonic energies using the linear band model can be calculated using a variational approach as it was done in the last section. In this case however, one has to determine the energy from Eqn. 3.56. Due to Parseval's theorem (App. D) the energy expectation value is preserved. This means that

$$\int |\Psi_{\text{exc}}(\boldsymbol{r})|^2 \, d^2r = \int |\Psi_{\boldsymbol{k}}|^2 \, d^2k \tag{4.12}$$

Since the wave function is normalized the left hand side is equal to unity. Thus, the right hand side is also equal to unity, corresponding to the obvious fact that the probability of finding the exciton with some momentum between zero and infinity is unity. The kinetic energy terms

of Eqn. 3.56 are evaluated in $\boldsymbol{k}$-space while the potential energy term is evaluated in $\boldsymbol{r}$-space according to

$$E_{\text{kin}} = \int \sqrt{\alpha^2 + \gamma_c^2 k^2} \left| \Psi_{vc\boldsymbol{k}} \right|^2 k \, d^2k + \int \sqrt{\alpha^2 + \gamma_v^2 k^2} \left| \Psi_{vc\boldsymbol{k}} \right|^2 k \, d^2k \tag{4.13}$$

$$E_{\text{pot}} = \int \frac{V(\boldsymbol{r})}{\varepsilon(\boldsymbol{r})} \left| \Psi_{\text{exc}}(\boldsymbol{r}) \right|^2 r \, d^2r \tag{4.14}$$

To proceed with the variational estimate of the binding energies an expression for the wave function is needed. The ansatz used for the effective mass case in the last section is again used

$$\Psi_{\text{exc}}(r) = 2\eta e^{-\eta r} \tag{4.15}$$

This is plotted for $\eta = 1$ in the right part of Fig. 4.5 where it can be seen that this ansatz allows the electron and the hole to be very close to each other.
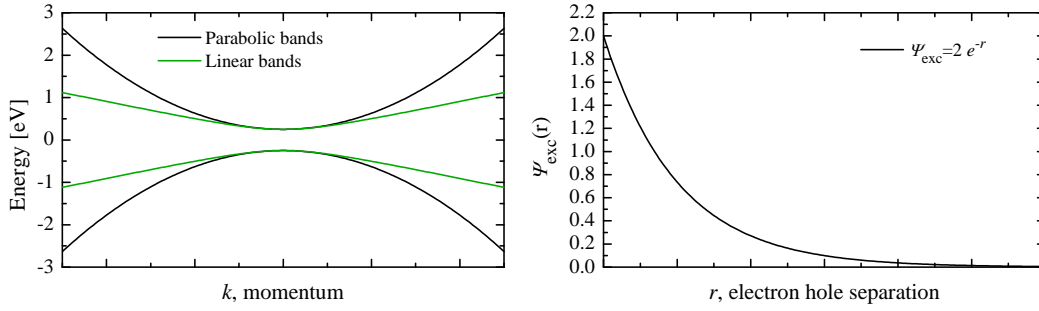

Figure 4.5: (left) Diagram of parabolic bands versus linear bands. Here it is seen that the energy increases faster for the parabolic bands than for the linear bands as a function of the momentum. Linear bands thus allows for higher momentum. (right) The ansatz for the wavefunction.

Using this ansatz is not without complications though. Due to the linear energy dispersion the electron and the hole are allowed to have larger momentum than for parabolic bands because the energy penalty paid is not as large as for the parabolic bands. This is illustrated in the left part of Fig. 4.5. Larger k values mean smaller separation between the electron and the hole which is favoured due to the Coulomb attraction. The kinetic energy penalty paid due to the larger momentum is not large enough to keep the electron and the hole separated and so the exciton collapses and the energy diverges. In practice this means that below some critical value of the band gap the ansatz Eqn. 4.15 does not show a minimum for any value of the variational parameter η. Using a higher value of the screening causes the Coulomb energy to decrease and thus the exciton does not collapse. In this way non divergent binding energies can be obtained.

In order to calculate the kinetic energy for this ansatz the Fourier transform is needed. The 2D Fourier transform of a circularly symmetric function $R(r)$ can be calculated in the following way

$$\tilde{R}(\boldsymbol{k}) = \frac{1}{2\pi} \iint R(r)e^{i\boldsymbol{k}\cdot\boldsymbol{r}} dxdy$$

$$= \frac{1}{2\pi} \iint R(r)e^{ikr\cos\theta} rdrd\theta$$

$$= \frac{1}{2\pi} \int R(r) \left[\int e^{ikr\cos\theta} d\theta \right] rdr$$

$$= \int R(r)J_0(kr)rdr \qquad (4.16)$$

which is just the zero'th order Hankel transform (also known as the Fourier-Bessel transform). The Fourier transform is therefore also circularly symmetric. Thus, the Fourier transform of the ansatz Eqn. 4.15 becomes

$$\Psi_{\boldsymbol{k}} = \int \Psi_{\mathrm{exc}}(r)J_0(kr)rdr = \frac{2\eta^2}{\left(\eta^2 + k^2\right)^{3/2}} \qquad (4.17)$$

With this expression for the Fourier transform one can calculate the kinetic energy from Eqn. 4.13 and using the ansatz Eqn. 4.15 the potential energy can be calculated from Eqn. 4.14. The optimal value of η, the value which minimizes the total energy, can then be found. Using the simple approximation for the screening, i.e., assuming that the screening is a constant, the binding energies can be calculated. In order to obtain non divergent binding energies the screening must be large enough that the exciton does not collapse. The screening is set to $\varepsilon = 5.0$. This gives the following binding energies calculated with the Wannier model using linear bands

$$E_{B,81}^{\mathrm{lin}} = -11\,\mathrm{meV} \qquad E_{B,250}^{\mathrm{lin}} = -47\,\mathrm{meV} \qquad E_{B,358}^{\mathrm{lin}} = -84\,\mathrm{meV} \qquad E_{B,569}^{\mathrm{lin}} = -132\,\mathrm{meV}$$
$$E_{B,577}^{\mathrm{lin}} = \mathrm{div.} \qquad E_{B,409}^{\mathrm{lin}} = \mathrm{div.}$$

where the superscript "lin" means that these values are calculated using linear bands and "div." means that the binding energy is divergent for the relevant structure. For comparison, the binding energies calculated using the Wannier model with the effective mass approximation and a screening of $\varepsilon = 5.0$ are

$$E_{B,81}^{\varepsilon=5.0} = -8\,\mathrm{meV} \qquad E_{B,250}^{\varepsilon=5.0} = -34\,\mathrm{meV} \qquad E_{B,358}^{\varepsilon=5.0} = -54\,\mathrm{meV} \qquad E_{B,569}^{\varepsilon=5.0} = -97\,\mathrm{meV}$$
$$E_{B,577}^{\varepsilon=5.0} = -373\,\mathrm{meV} \qquad E_{B,409}^{\varepsilon=5.0} = -206\,\mathrm{meV}$$

For the two structures with $E_g = 577$ and $E_g = 409$ the binding energy again diverges in the linear band model and the energy does not show a minimum for any value of η. The slope of the bands for these structures is about a factor of 2-3 smaller than the slope of the band for the other structures, which again makes it energetically too "cheap" to increase the momentum and thereby decrease the electron-hole separation. The most important conclusion to make for these results is that the binding energy increases (becomes more negative) in the linear band model because the electron and the hole are allowed to be closer to each other.

4.3   Antidot geometry

In order to investigate the influence of the antidot geometry the band gap dependence on the antidot lattice geometry is investigated. The band gaps in the two geometries will be compared in order to determine the influence of the geometry on the band gap.

Setting up the hexagonal lattice

In order to apply the TB method the coordinates of the atoms within the unit cell have to be known. In this section it is shown how to generate the geometry of the antidot lattice. For the purpose of illustrating the setup of the unit cell geometry, i.e., to find the coordinates of the atoms in the unit cell, unit cells without holes in them will be considered first. The introduction of holes into the unit cells is discussed later.

To determine the coordinates of the atoms in the unit cell the lines which bound the unit cell are first defined. These lines are shown as dashed lines surrounding the unit cell for a hexagonal lattice in the left part of Fig. 4.6. To create the unit cell geometry one simply checks all points among a set of points which is certain to contain the whole unit cell. If the point lies inside the structure defined by the lines, it belongs to the unit cell. Any point can be transformed into the first quadrant by taking the absolute value of x and y. Due to symmetry reasons, it is enough to check if the transformed point lies within the area bounded by the x and y axes and the two lines L1 and L2 in order to determine if the point belongs to the unit cell.

The lines are defined in terms of the unit cell size. The size of the unit cell is defined by the edge length, L, and the edge length is expressed in terms of the number of hexagons on the unit cell edge. For example, the structure shown in the left part of the figure has an edge length of $L = 3$. The actual length of the unit cell edge in Ångstrøms is given by La_0 where $a_0 = 2.46$Å is the graphene lattice constant. The lines L1 and L2 are defined by

$$\text{L1:} \quad y = -\frac{x}{\sqrt{3}} + La_0 \tag{4.18}$$

$$\text{L2:} \quad x = \frac{\sqrt{3}}{2}La_0 \tag{4.19}$$

The condition for a point (x, y) being inside the unit cell then becomes

$$|x| < \frac{\sqrt{3}}{2}La_0 \quad \text{and} \quad |y| < -\frac{x}{\sqrt{3}} + La_0 \tag{4.20}$$

With the positions of the atoms within the unit cell specified, it still remains to specify the lattice. The lattice vectors are given by

$$\boldsymbol{a}_1 = \left(\frac{\sqrt{3}}{2}, \frac{3}{2}\right) La_0, \qquad \boldsymbol{a}_2 = \left(\frac{\sqrt{3}}{2}, -\frac{3}{2}\right) La_0 \tag{4.21}$$

No single atom is shared between two or more unit cells. Each atom in the crystal belongs to one and only one unit cell. This is important because in the TB model it must be specified
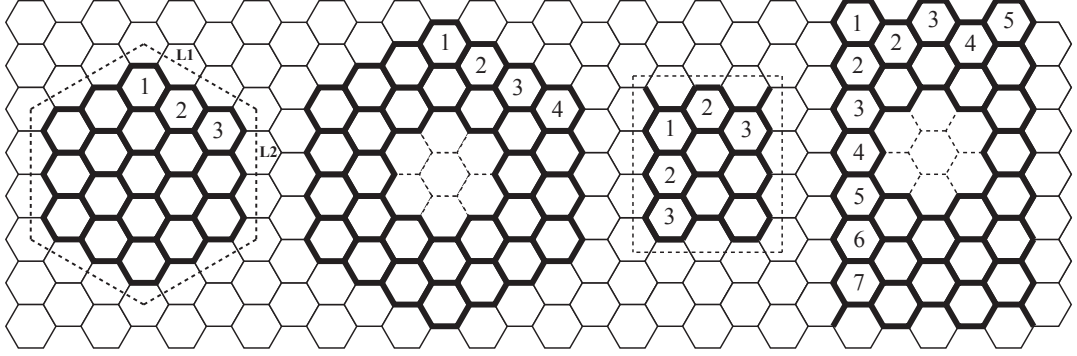
Figure 4.6: Unit cells of the hexagonal and the rectangular lattice. The two leftmost unit cells are for a {3,0} and a {4,1} hexagonal antidot lattice respectively. The two rightmost unit cells are for rectangular lattices {3,3,0} and {5,7,1}. The numbers on the edges of the unit cells indicate the size of the unit cells.

which types of atom each atom interacts with. Each atom in the unit cell is given a unique number but if the atom is shared among several unit cells it is unclear which type of atom it is. In order to avoid these complications the unit cells are chosen as shown.

In order to calculate the band structure it is necessary to know the reciprocal lattice vectors. They can be calculated by the requirement that $e^{i\boldsymbol{a}_i \cdot \boldsymbol{b}_j} = 1$ from which it follows that $\boldsymbol{a}_i \cdot \boldsymbol{b}_j = 2\pi\delta_{ij}$. By exploiting this relationship the reciprocal lattice vectors are found to be

$$\boldsymbol{b}_1 = \left(\frac{1}{\sqrt{3}}, \frac{1}{3}\right)\frac{2\pi}{La_0}, \qquad \boldsymbol{b}_2 = \left(\frac{1}{\sqrt{3}}, -\frac{1}{3}\right)\frac{2\pi}{La_0} \tag{4.22}$$

The introduction of holes into the unit cell is simply a matter of removing atoms from the middle of the unit cell. To create a circular hole atoms with coordinates which satisfy $x^2 + y^2 < (Ra_0)^2$, where R is the hole radius and not necessarily an integer, are removed. The hole radius is thus expressed in terms of a_0 just as the edge length.

Setting up the square/rectangular lattice

The procedure for setting up the square/rectangular antidot lattice does not differ much from the procedure described above. The lines bounding the unit cell are defined and all atoms within the bounds belong to the unit cell. In contrast to the hexagonal lattice, where the unit cell is characterized by a side length and hole diameter, the unit cell in the square lattice is determined by a height, a width, and a hole diameter. A lattice in the rectangular configuration is designated as $\{L_x, L_y, R\}$ where L_x is the width measured in the armchair direction, L_y is the height measured in the zig-zag direction and R is the hole radius. Due to the symmetry of the underlying graphene lattice a perfectly square antidot lattice cannot be constructed. An almost square lattice can be made however, and the discrepancy becomes smaller for large unit cells. The lattice vectors for the rectangular lattice are given by

$$\boldsymbol{a}_1 = \left(\frac{3 + 3L_x}{2}, \quad 0\right)\frac{a_0}{\sqrt{3}}, \qquad \boldsymbol{a}_2 = \left(0, \quad 2(L_y + 1)\right)\frac{a_0}{2} \tag{4.23}$$

where L_x is the unit cell width measured in the armchair direction and L_y is the unit cell height measured in the zig-zag direction. Antidot lattices in the rectangular geometry are designated as $\{L_x, L_y, R\}$, where R is the radius of the hole. The corresponding reciprocal lattice vectors are given as

$$\boldsymbol{b}_1 = \left(\frac{4\pi}{\sqrt{3}a_0(1+L_x)}, \quad 0 \right), \qquad \boldsymbol{b}_2 = \left(0, \frac{2\pi}{a_0(1+L_y)} \right) \tag{4.24}$$

An example of a rectangular lattice is shown in Fig. 1.3(b). The Brillouin zone in this geometry is rectangular just as the direct lattice. In Fig. 4.6 two unit cells of the rectangular lattice are shown. In order to obtain a lattice as close to a square lattice (not rectangular) as possible one must, for the lattice vectors chosen, require that

$$\frac{|\boldsymbol{a}_1|}{|\boldsymbol{a}_2|} = \frac{\sqrt{3}(1+L_x)}{2(1+L_y)} \approx 1 \tag{4.25}$$

which yields the following expression for L_y

$$L_y = \text{round}\left[\frac{1}{2}(\sqrt{3}L_x + \sqrt{3} - 2) \right] \tag{4.26}$$

where the result has to be rounded because non-integer values of L_y are meaningless. Using this expression for L_y an almost square antidot lattice is obtained.

Results

In the context of square and rectangular antidot lattices it is interesting to know how the band gap is influenced by the parameters of the lattice, that is, the unit cell width and height and the hole size. In Tbl. 4.2 the band gaps for structures of a constant width 11, hole radius 2.0 and heights ranging between 5 and 24 are shown. Here it is seen that the band gap is only appreciable for structures with unit cell heights obeying $L_y = 2 + 3n$ with $n = 0, 1, 2\ldots$, and this pattern continuous for even larger structures of height 24 and beyond (not shown in the table). Most of the structures in the table with an indicated band gap of 0.0 eV do in fact have a small band gap on the order of 1-5 meV.

In the case of hexagonal antidot lattices the band gap is always located at the Γ point in the Brillouin zone independently of the size of the unit cell or the diameter of the hole. In the case of rectangular antidot lattices the band gap is not fixed in the Brillouin zone. In some cases it is located somewhere between high symmetry points of the Brillouin zone. This is because the unit cell geometry does not follow the geometry of the underlying graphene lattice as it does in the case of hexagonal lattices.

If the unit cell height is held constant and the width is varied the gap decreases with increasing width. This is shown in Tbl. 4.3. The tendencies just described are seen for all structures and for all hole sizes, they are however, more pronounced when the ratio of number of removed atoms to total number of atoms is small.

In Fig. 4.7 the band gaps for several antidot structures in both the hexagonal and the square geometry are plotted as a function of $N_{\text{rem}}^{1/2}/N_{\text{tot}}$, the ratio of the square root of number of

Antidot lattice	Total atoms	Removed atoms	Gap [eV]
{11,5,2.0}	144	24	0.77
{11,6,2.0}	168	24	0.00
{11,7,2.0}	192	24	0.08
{11,8,2.0}	216	24	0.54
{11,9,2.0}	240	24	0.00
{11,10,2.0}	264	24	0.04
{11,11,2.0}	288	24	0.42
{11,12,2.0}	312	24	0.00
{11,13,2.0}	336	24	0.04
{11,14,2.0}	360	24	0.34
{11,15,2.0}	384	24	0.00
{11,16,2.0}	408	24	0.03
{11,17,2.0}	432	24	0.28
{11,18,2.0}	456	24	0.00
{11,19,2.0}	480	24	0.03
{11,20,2.0}	504	24	0.23
{11,21,2.0}	528	24	0.00
{11,22,2.0}	552	24	0.03
{11,23,2.0}	576	24	0.21
{11,24,2.0}	600	24	0.00

Table 4.2: Band gap as a function of unit cell height (hole separation in zig-zag direction) with the unit cell width (hole separation in armchair direction) and the hole size held constant.

Antidot lattice	Total atoms	Removed atoms	Gap [eV]
{5,8,2.0}	108	24	0.64
{7,8,2.0}	144	24	0.67
{9,8,2.0}	180	24	0.62
{11,8,2.0}	216	24	0.54
{13,8,2.0}	252	24	0.48
{15,8,2.0}	288	24	0.42
{17,8,2.0}	324	24	0.38

Table 4.3: Band gap as a function of unit cell width (hole separation in the armchair direction) with the unit cell height (hole separation in the zig-zag direction) and the hole size held constant.
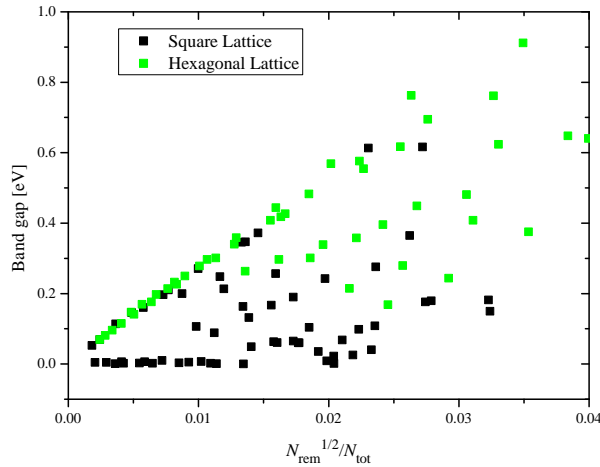
Figure 4.7: Band gap for various antidot structures in both hexagonal and square hole geometries.

removed atoms to total number of atoms. This plot clearly shows that the band gap in the rectangular geometry in many cases becomes much smaller than the band gap in a corresponding hexagonal lattice. Here an antidot lattice in the hexagonal geometry is said to correspond to an antidot lattice in the rectangular geometry if the ratio $N_{\text{rem}}^{1/2}/N_{\text{tot}}$ is approximately the same in the two. From the figure it is seen that the presence of a gap is highly dependent on that ratio. For two rectangular antidot lattices of nearly the same ratio one might have a relatively large gap while the other have zero gap. According to the discussion above, rectangular antidot lattices have appreciable gaps for small ratios only if the unit cell height obeys $L_y = 2 + 3n$ with $n = 0, 1, 2\ldots$, which explains the very rapid oscillations in the gap size in Fig. 4.7.

For those rectangular antidot lattices with small $N_{\text{rem}}^{1/2}/N_{\text{tot}}$ ratios which do have an appreciable gap, an approximately linear relationship between ratio and gap is seen, just as for the hexagonal lattice. An approximate expression for the linear behaviour is given by

$$E_g(x) \approx 0.0036\,[\,\text{eV}\,] + 27.23\,[\,\text{eV}\,]\,x \qquad (4.27)$$

These results for rectangular lattices are important because they show that rectangular lattices with band gaps are difficult to realize in practice. The very heavy dependence on the ratio of removed atoms to total number of atoms means that small deviations in the production could cause the gap to disappear. For hexagonal lattices one does not see the same heavy dependence on the ratio between removed atoms and total number of atoms, which means that hexagonal lattices is a better approach to making antidot lattices in order to introduce a gap into graphene.

In [13] square antidot lattices have been fabricated, although, with a much larger lattice constant and hole size than the structures which have been treated here. In [13] gaps on the order of 6 meV are found. The calculations made in this work suggests that some rectangular/square antidot lattices have either zero gap or a very small gap which is in accordance with the experimental results. If the linear relationship between the gap and the characteristic ratio is extended to antidot lattices as the ones fabricated a gap of approximately 25 meV is deduced. More work is however required in order to make any conclusions. The following questions need

to be addressed

1. How does defects influence the band gap in the rectangular geometry.

2. How does the much larger unit cell size in the experiments affect the band gap.

3. What is the explanation of the peculiar behaviour of the band gap seen in Tbl. 4.2.

Chapter 5

Discussion and conclusion

In this work graphene antidot lattices have been investigated and the following issues have been addressed

1. How are the exciton binding energies influenced when the assumption that only the surroundings contribute to the screening in the graphene layer is abandoned, and the screening from the graphene layer itself is included in the calculation?

2. How are the exciton binding energies influenced when the effective mass approximation is abandoned and the linear band dispersion is used?

3. How is the band gap influenced when the hole geometry in an antidot lattice is changed from a hexagonal lattice to a rectangular/square lattice?

The first point has been addressed by solving the Poisson equation for the two interface system and using a model based on time dependent perturbation theory for the dielectric function of the graphene layer. Earlier work yielded unphysical large exciton binding energies, and it is expected that part of the discrepancy is due to the very rough calculation of the screening in the graphene layer which was employed. The findings of this work is that the more advanced model of the screening, allowing for the screening to be spatially varying, reduces the binding energy by a factor of ≈ 2.6. The dependence of the real space dielectric function in Fig. 4.3 on the distance between the two charges show that the screening is nonlocal. This nonlocality causes the simple model in which the screening is assumed to be a constant determined solely by the surroundings to break down. The more advanced model employed in this work solves part of the discrepancies, but for some structures, in particular structures with large holes compared to the unit cell size, the binding energies are still unphysical large.

The second point has been answered by employing the Wannier model with linear dispersive bands. A variational approach was used and the kinetic energy terms was calculated in $\boldsymbol{k}$-space while the potential energy was calculated in $\boldsymbol{r}$-space. It was found that for some structures the binding energy diverges while for others it was increased compared to the one calculated using the effective mass approximation with $\varepsilon = 5.0$.

The third point has been investigated by modelling rectangular antidot lattices in the quasi-particle tight binding model as it has been done for hexagonal lattices earlier. The findings here are somewhat surprising since the presence of a band gap is highly dependent on the details of the structure. Thus, for some rectangular lattices a large or moderate gap is found

while for others the gap is vanishing. It has been shown that a non vanishing gap is present for structures with unit cell heights obeying $L_y = 2 + 3n$ where the height is measured in the zig-zag direction of the graphene lattices. The presence of a gap does not show the same strong dependence as a function of the unit cell width, which is measured in the armchair direction. In this case the band gap merely decreases when the width increases since the hole becomes an increasingly smaller perturbation. This is similar to what is seen for hexagonal lattices. For heights obeying the aforementioned rule, the gap size does decrease as a function of width. To uncover the reason for the somewhat peculiar behaviour of rectangular lattices further investigations have to be made.

In conclusion, the goal of this thesis has been achieved. A more advanced model for screening in graphene has been applied and part of the discrepancies seen in the more simple model has been removed. Square antidot lattices have been investigated and it has been found that the band gap is highly dependent on the details of the structure.

Appendix A

Derivation of nonlocal conductivity

The derivation of the nonlocal conductivity starts from the continuity equation which states

$$\boldsymbol{\nabla} \cdot \boldsymbol{J} = -\frac{d\rho}{dt} \tag{A.1}$$

where $\boldsymbol{J}$ is the current density and $\rho(\boldsymbol{r})$ is the charge density. The current density is given by $\boldsymbol{J} = \sigma \boldsymbol{E} = \sigma \boldsymbol{\nabla} U / |e|$, where U is the potential energy, and so the continuity equation becomes

$$\sigma \nabla^2 U = -|e| \frac{d\rho}{dt} \tag{A.2}$$

Expanding the potential and the charge density as a Fourier series in the following way (see App. D)

$$U(\boldsymbol{r}) = \frac{\Omega}{4\pi^2} \int_{\boldsymbol{q}} \tilde{U}(\boldsymbol{q}) e^{i\boldsymbol{q}\cdot\boldsymbol{r}} d^2 q \tag{A.3}$$

$$\rho(\boldsymbol{r}) = \frac{\Omega}{4\pi^2} \int_{\boldsymbol{q}} \tilde{\rho}(\boldsymbol{r}, \boldsymbol{q}) e^{i\boldsymbol{q}\cdot\boldsymbol{r}} d^2 q \tag{A.4}$$

and inserting this into the continuity equation, one obtains

$$\sigma \int_{\boldsymbol{q}} \tilde{U} q^2 e^{i\boldsymbol{q}\cdot\boldsymbol{r}} d^2 q = |e| \int_{\boldsymbol{q}} \frac{d\tilde{\rho}}{dt} e^{i\boldsymbol{q}\cdot\boldsymbol{r}} d^2 q \tag{A.5}$$

Since this equation must be fulfilled for all $\boldsymbol{r}$ (the continuity equation has to be fulfilled at all points in space), one must require the Fourier coefficients on both sides to be equal

$$\sigma q^2 \tilde{U} = |e| \frac{d\tilde{\rho}}{dt} \tag{A.6}$$

and thus

$$\tilde{\sigma}(\boldsymbol{q}) = \frac{|e|}{q^2 \tilde{U}} \frac{d\tilde{\rho}}{dt} \tag{A.7}$$

Fourier transforming the charge density in time as well, one obtains the following expression for the Fourier components of the conductivity

$$\tilde{\sigma}(\omega, \boldsymbol{q}) = -\frac{i\omega |e|}{q^2 \tilde{U}} \tilde{\rho} \tag{A.8}$$

In order to calculate the conductivity the Fourier component of the charge density is needed. The charge density can be calculated by exploiting a result from time dependent linear response theory

$$X(\omega) = -\sum_{m,n} f_{nm} \frac{\langle \varphi_m | \hat{H} | \varphi_n \rangle \langle \varphi_n | \hat{X} | \varphi_m \rangle}{E_{mn} - \hbar\omega - i\hbar\Gamma} \tag{A.9}$$

where φ_m and φ_n are single particle wave functions, $f_{nm} = f(E_n) - f(E_m)$ is the Fermi occupation function, $E_{mn} = E_m - E_n$ and Γ a damping related to energy losses in the system. The summation covers all accessible states of the system. $\hat{X}$ is the operator associated with the observable $X(\omega)$ and $\hat{H}$ is the interaction of the perturbation with the system. In order to calculate the induced charge density due to an external field oscillating at a frequency ω the operators for the interaction and the observable are

$$\hat{H} = U(\boldsymbol{r}) \tag{A.10}$$

$$\hat{X} = -|e|\, \delta(\boldsymbol{r} - \boldsymbol{r}') \tag{A.11}$$

The operator for the charge density gives the charge density at $\boldsymbol{r}$ due to an electron at $\boldsymbol{r}'$. The charge density then becomes

$$\tilde{\rho}(\omega, \boldsymbol{r}') = |e| \sum_{m,n} f_{nm} \frac{\langle \varphi_m | U(\boldsymbol{r}) | \varphi_n \rangle \varphi_n^*(\boldsymbol{r}') \varphi_m(\boldsymbol{r}')}{E_{mn} - \hbar\omega - i\hbar\Gamma} \tag{A.12}$$

The potential $U(r)$ is completely general so that this formula provides the charge density for a temporally and spatially varying perturbation, with the restriction that the perturbation has to be monochromatic. Expanding the potential as a Fourier series as it was done in Eqn. A.4 but looking only at a single Fourier component

$$U(r) = \tilde{U}(\boldsymbol{q})e^{i\boldsymbol{q}\cdot\boldsymbol{r}} \tag{A.13}$$

and inserting this into Eqn. A.12

$$
\begin{aligned}
\tilde{\rho}(\omega, \boldsymbol{r}') &= |e|\,\tilde{U} \sum_{m,n} f_{nm} \frac{\langle\varphi_m|\, e^{i\boldsymbol{q}\cdot\boldsymbol{r}}\,|\varphi_n\rangle\,\varphi_n^*(\boldsymbol{r}')\varphi_m(\boldsymbol{r}')}{E_{mn} - \hbar\omega - i\hbar\Gamma} \\
&= |e|\,\tilde{U} \int_{\boldsymbol{r}} \sum_{m,n} f_{nm} \frac{\varphi_m^*(\boldsymbol{r})\varphi_n(\boldsymbol{r})\varphi_n^*(\boldsymbol{r}')\varphi_m(\boldsymbol{r}')}{E_{mn} - \hbar\omega - i\hbar\Gamma} e^{i\boldsymbol{q}\cdot\boldsymbol{r}}d^2r \\
&= |e|\,\tilde{U} \int_{\boldsymbol{r}} \chi(\boldsymbol{r},\boldsymbol{r}')e^{i\boldsymbol{q}\cdot\boldsymbol{r}}d^2r \tag{A.14}
\end{aligned}
$$

Fourier transforming with respect to the $\boldsymbol{r}'$ coordinate, the Fourier component of the charge density is obtained

$$\tilde{\rho}(\omega, \boldsymbol{q}) = |e|\,\tilde{U}\frac{1}{\Omega}\left(\int_{\boldsymbol{r}}\int_{\boldsymbol{r}'} \chi(\boldsymbol{r},\boldsymbol{r}')e^{i\boldsymbol{q}\cdot(\boldsymbol{r}-\boldsymbol{r}')}d^2rd^2r'\right) \tag{A.15}$$

Inserting the $\boldsymbol{q}$ dependent charge density into the expression for the conductivity, Eqn. A.8

$$
\begin{aligned}
\tilde{\sigma}(\omega, \boldsymbol{q}) &= -\frac{i\omega e^2}{q^2}\frac{1}{\Omega}\left(\int_{\boldsymbol{r}}\int_{\boldsymbol{r}'} \chi(\boldsymbol{r},\boldsymbol{r}')e^{i\boldsymbol{q}\cdot(\boldsymbol{r}-\boldsymbol{r}')}d^2rd^2r'\right) \\
&= -\frac{i\omega e^2}{q^2}\frac{1}{\Omega}\sum_{m,n} f_{nm}\frac{\langle\varphi_m|\, e^{i\boldsymbol{q}\cdot\boldsymbol{r}}\,|\varphi_n\rangle\,\langle\varphi_n|\, e^{-i\boldsymbol{q}\cdot\boldsymbol{r}}\,|\varphi_m\rangle}{E_{mn} - \hbar\omega - i\hbar\Gamma} \\
&= -\frac{i\omega e^2}{q^2}\frac{1}{\Omega}\sum_{m,n} f_{nm}\frac{\left|\langle\varphi_m|\, e^{i\boldsymbol{q}\cdot\boldsymbol{r}}\,|\varphi_n\rangle\right|^2}{E_{mn} - \hbar\omega - i\hbar\Gamma} \tag{A.16}
\end{aligned}
$$

In this expression the summations over m and n are over all valence band states and all conduction band states. In a crystal there will be many conduction and valence band states each indexed by a different value of the momentum $\boldsymbol{k}'$, where the prime is used to indicate that the different spin states are contained within the $\boldsymbol{k}'$ summation ($\boldsymbol{k}'$ denotes a spin-momentum state). All these states in a particular conduction or valence band are denoted collectively by c' and v' respectively, so that $v' = 1$ denotes all the states of different $\boldsymbol{k}'$ belonging to this particular valence band. The summation above can be split as follows

$$\sum_{m,n} = \sum_{m\in v'}\sum_{n\in v'} + \sum_{m\in c'}\sum_{n\in c'} + \sum_{m\in c'}\sum_{n\in v'} + \sum_{m\in v'}\sum_{n\in c'} \tag{A.17}$$

For the first two summations the occupation factor f_{nm} is practically zero. The two summations correspond to the contribution to the conductivity from excitations from a valence band to

another valence band and from a conduction band to another conduction band respectively. The probability of these transitions is very low at moderate temperatures. Using $E_{mn} = -E_{nm}$ and $f_{nm} = -f_{mn}$ and exchanging the indices in the last summation (so that m runs over conduction band states and n runs over valence band states) one obtains

$$\tilde{\sigma}(\omega, \boldsymbol{q}) = -\frac{i2\omega e^2}{q^2} \frac{1}{\Omega} \sum_{m \in c'} \sum_{n \in v'} \frac{E_{mn} \left| \langle \varphi_m | e^{i\boldsymbol{q} \cdot \boldsymbol{r}} | \varphi_n \rangle \right|^2}{E_{mn}^2 - (\hbar\omega + i\hbar\Gamma)^2} \qquad (A.18)$$

The sums here run over all valence band states and all conduction band states. Writing out the sums as sums over bands and sums over spin-momentum

$$\tilde{\sigma}(\omega, \boldsymbol{q}) = -\frac{i2\omega e^2}{q^2} \frac{1}{\Omega} \sum_{m \in c} \sum_{n \in v} \sum_{\boldsymbol{k}'_c} \sum_{\boldsymbol{k}'_v} \frac{E_{mn} \left| \langle \varphi_m(\boldsymbol{k}'_c) | e^{i\boldsymbol{q} \cdot \boldsymbol{r}} | \varphi_n(\boldsymbol{k}'_v) \rangle \right|^2}{E_{mn}^2 - (\hbar\omega + i\hbar\Gamma)^2} \qquad (A.19)$$

Since the operator $e^{i\boldsymbol{q} \cdot \boldsymbol{r}}$ is independent of spin, the matrix element vanishes whenever the two states differ in spin. Thus, the spin summation gives simply a factor of two, i.e. $\sum_{\boldsymbol{k}'_c} \sum_{\boldsymbol{k}'_v} = 2\sum_{\boldsymbol{k}_c} \sum_{\boldsymbol{k}_v}$. Now, according to the Bloch theorem the states in a crystal are given by

$$\varphi_m(\boldsymbol{k}_c) = u_m(\boldsymbol{k}_c)e^{i\boldsymbol{k}_c \cdot \boldsymbol{r}} \qquad (A.20)$$
$$\varphi_n(\boldsymbol{k}_v) = u_n(\boldsymbol{k}_v)e^{i\boldsymbol{k}_v \cdot \boldsymbol{r}} \qquad (A.21)$$

States of different $\boldsymbol{k}$ are orthogonal and therefore the matrix element vanish for states which do not obey $\boldsymbol{k}_c = \boldsymbol{q} + \boldsymbol{k}_v$. This effectively removes one of the $\boldsymbol{k}$ sums and one is left with

$$\tilde{\sigma}(\omega, \boldsymbol{q}) = -\frac{i4\omega e^2}{q^2} \frac{1}{\Omega} \sum_{m \in c} \sum_{n \in v} \sum_{\boldsymbol{k}} \frac{E_{mn} \left| \langle \varphi_m(\boldsymbol{k} + \boldsymbol{q}) | e^{i\boldsymbol{q} \cdot \boldsymbol{r}} | \varphi_n(\boldsymbol{k}) \rangle \right|^2}{E_{mn}^2 - (\hbar\omega + i\hbar\Gamma)^2} \qquad (A.22)$$

Since the crystal is for all practical purposes infinite in the plane, the $\boldsymbol{k}$ states lie infinitely close together. Therefore the $\boldsymbol{k}$ summation can be replaced by an integral

$$\tilde{\sigma}(\omega, \boldsymbol{q}) = -\frac{i\omega e^2}{\pi^2 q^2} \sum_{m \in c} \sum_{n \in v} \int \frac{E_{mn} \left| \langle \varphi_m(\boldsymbol{k} + \boldsymbol{q}) | e^{i\boldsymbol{q} \cdot \boldsymbol{r}} | \varphi_n(\boldsymbol{k}) \rangle \right|^2}{E_{mn}^2 - (\hbar\omega + i\hbar\Gamma)^2} d^2k \qquad (A.23)$$

The absorption of the material is given by the real part of the conductivity. Due to the imaginary i outside the sums, the contribution to the real part comes from the imaginary part of the integrand. Since the nominator is always real, the only contribution to the imaginary part comes from the denominator of the integrand,

$$\frac{1}{(E_{mn})^2 - \hbar^2(\omega + i\Gamma)^2} = \frac{1}{[E_{mn} - \hbar(\omega + i\Gamma)][E_{mn} + \hbar(\omega + i\Gamma)]} \qquad (A.24)$$

Splitting the fraction into partial fractions according to

$$\frac{1}{[E_{mn} - \hbar(\omega + i\Gamma)][E_{mn} + \hbar(\omega + i\Gamma)]} = \frac{A}{E_{mn} - \hbar(\omega + i\Gamma)} + \frac{B}{E_{mn} + \hbar(\omega + i\Gamma)} \qquad (A.25)$$

the constants A and B can thus be determined (more than one solution exists) and they are given by $A = 1/(2E_{mn})$ and $B = 1/(2E_{mn})$. Therefore, after some algebra

$$\text{Im}\left[\frac{1}{(E_{mn})^2 - \hbar^2(\omega + i\Gamma)^2}\right] = \frac{1}{2E_{mn}}\left[\frac{\hbar\Gamma}{(E_{mn} - \hbar\omega)^2 + \hbar^2\Gamma^2} - \frac{\hbar\Gamma}{(E_{mn} + \hbar\omega)^2 + \hbar^2\Gamma^2}\right] \qquad (A.26)$$

As the broadening Γ tends to zero in the above expression the last term on the right hand side goes to zero and only the first term persists. For this term one gets

$$\frac{1}{2E_{mn}}\lim_{\Gamma\to 0}\left[\frac{\hbar\Gamma}{(E_{mn} - \hbar\omega)^2 + \hbar^2\Gamma^2}\right] = \frac{\pi}{2E_{mn}}\delta(E_{mn} - \hbar\omega) \qquad (A.27)$$

This gives, for the real part of the complex conductivity

$$\text{Re}\left[\tilde{\sigma}(\omega, \boldsymbol{q})\right] = \frac{\omega e^2}{2\pi q^2}\sum_{m\in c}\sum_{n\in v}\int \left|\langle\varphi_m(\boldsymbol{k}+\boldsymbol{q})|\,e^{i\boldsymbol{q}\cdot\boldsymbol{r}}\,|\varphi_n(\boldsymbol{k})\rangle\right|^2 \delta(E_{mn} - \hbar\omega)d^2k \qquad (A.28)$$

In terms of the graphene minimum conductivity, $\sigma_0 = e^2/(4\hbar)$ the conductivity is

$$\text{Re}\left[\tilde{\sigma}(\omega, \boldsymbol{q})\right] = \sigma_0\frac{2\hbar\omega}{\pi q^2}\sum_{m\in c}\sum_{n\in v}\int \left|\langle\varphi_m(\boldsymbol{k}+\boldsymbol{q})|\,e^{i\boldsymbol{q}\cdot\boldsymbol{r}}\,|\varphi_n(\boldsymbol{k})\rangle\right|^2 \delta(E_{mn} - \hbar\omega)d^2k \qquad (A.29)$$

Appendix B

Tight binding theory

The tight binding (TB) method is a method used for calculation of electronic band structures of solids. It is an LCAO (linear combination of atomic orbitals) approach to determining the total wave function of the crystal, similar to the LCAO approach used for example when calculating energy levels in atoms. The idea in the LCAO approach is that the complicated unknown wave function can be written as a linear combination of relatively simple known wave functions. For example, in determining the wave function of atoms with $Z > 1$ the wave function is expanded in terms of hydrogenic orbitals which can be obtained analytically. The problem is then a matter of customizing the orbitals to the specific situation and determining the weighing coefficient of each of the hydrogenic orbitals. The last problem can be easily solved by using for example the Hartree-Fock method.

Several variants of TB exist ranging from ab-initio (from first principles) to semi-empirical methods. TB can be viewed as the counterpart to the nearly free electron model for which the plane wave basis is the most suited in describing the delocalized nature of the electrons. TB is used for description of electrons which are tightly bound to the nucleus and therefore the plane wave basis is not suitable. The wave function is instead expressed in terms of the wave functions of the localized orbitals which then constitute the basis. In semi-empirical TB an explicit expression for the localized orbitals is not needed, only the matrix elements are needed.

The wave function with band index j is expressed as

$$\Psi_{j\boldsymbol{k}}(\boldsymbol{r}) = \frac{1}{\sqrt{U}} \sum_p^N \sum_{lmn}^U b_{lmn,j}^p(\boldsymbol{k}) \ket{\varphi^p, \boldsymbol{R}_{lmn}^p} \tag{B.1}$$

where the first summation runs over all atoms of the unit cell (N) which may or may not be of the same type, and the second summation runs over all unit cells of the crystal (U). $\boldsymbol{R}_{lmn}^p = l\boldsymbol{a}_1 + m\boldsymbol{a}_2 + n\boldsymbol{a}_3 + \boldsymbol{r}_p$ is the position of atom p in the unit cell lmn, where r_p describes the atom position within the unit cell . $\ket{\varphi^p, \boldsymbol{R}_{lmn}^p}$ is the atomic orbital of type p centered at position $\boldsymbol{R}_{lmn}^p$. Now, according to the Bloch theorem [19] the wave function ψ of an electron in a periodic potential can be written as

$$\psi_{n\boldsymbol{k}}(\boldsymbol{r}) = e^{i\boldsymbol{k}\cdot\boldsymbol{r}} u_n(\boldsymbol{r}, \boldsymbol{k}) \tag{B.2}$$

Since, in Eqn. B.1 for a particular choice of p, the sum over lmn runs over atoms of the same type separated by $\boldsymbol{R}_{lmn} = l\boldsymbol{a}_1 + m\boldsymbol{a}_2 + n\boldsymbol{a}_3$, a vector of the lattice, this particular sum can be written as a Bloch function associated with atom p. Thus, a total of N Bloch functions exist, each given by

$$\Phi_{\boldsymbol{k}}^p(\boldsymbol{r}) = \frac{1}{\sqrt{U}} \sum_{lmn}^{U} e^{i\boldsymbol{k}\cdot\boldsymbol{R}_{lmn}^p} |\varphi^p, \boldsymbol{R}_{lmn}^p\rangle \tag{B.3}$$

By writing $b_{lmn}^p(\boldsymbol{k}) = c^p(\boldsymbol{k})e^{i\boldsymbol{k}\cdot\boldsymbol{R}_{lmn}^p}$ where $c^p(\boldsymbol{k})$, is the weight of the p'th Bloch function in the total wave function, Eqn. B.1 can be written as

$$\Psi_{j\boldsymbol{k}}(\boldsymbol{r}) = \sum_p^N c_j^p(\boldsymbol{k})\Phi_{\boldsymbol{k}}^p(\boldsymbol{r}) \tag{B.4}$$

The wave function has now been reexpressed in a basis of Bloch functions. In order to determine the coefficients $c_j^p(\boldsymbol{k})$ and the energies corresponding to each wave function, the wave function is inserted into the Schrödinger Equation (SE)

$$\hat{H}\Psi_{j\boldsymbol{k}}(\boldsymbol{r}) = E_j(\boldsymbol{k})\Psi_{j\boldsymbol{k}}(\boldsymbol{r}) \tag{B.5}$$

By using Eqn. B.4 one gets

$$\sum_p^N c_j^p(\boldsymbol{k})\hat{H}\Phi_{\boldsymbol{k}}^p(\boldsymbol{r}) = E_j(\boldsymbol{k})\sum_p^N c_j^p(\boldsymbol{k})\Phi_{\boldsymbol{k}}^p(\boldsymbol{r}) \tag{B.6}$$

Premultiplying by $\Phi_{\boldsymbol{k}}^{p'*}$ and integrating over all space gives

$$\sum_p^N c_j^p(\boldsymbol{k}) \langle\Phi_{\boldsymbol{k}}^{p'}| \hat{H} |\Phi_{\boldsymbol{k}}^p\rangle = E_j(\boldsymbol{k})\sum_p^N c_j^p(\boldsymbol{k}) \langle\Phi_{\boldsymbol{k}}^{p'}|\Phi_{\boldsymbol{k}}^p\rangle \tag{B.7}$$

Each particular choice of p' gives a new equation, so that there will be as many equations as there are atoms in the unit cell. This can be formulated as a generalized matrix problem

$$\hat{\mathsf{H}} \cdot \boldsymbol{c}_j = E_j(\boldsymbol{k})\hat{\mathsf{S}} \cdot \boldsymbol{c}_j \tag{B.8}$$

The matrix $\hat{\mathsf{H}}$ contains the matrix elements of the $\hat{H}$ operator and the matrix $\hat{\mathsf{S}}$ contains the overlap matrix elements. Both matrices are of dimension $N \times N$. The matrix elements can be determined by inserting the expressions for $\Phi_{\boldsymbol{k}}^p$ and $\Phi_{\boldsymbol{k}}^{p'}$, given by Eqn. B.3, into the expression for the matrix elements. One obtains then

$$\langle \Phi_{\boldsymbol{k}}^{p'} | \hat{H} | \Phi_{\boldsymbol{k}}^{p} \rangle = \frac{1}{U} \sum_{l'm'n'}^{U} \sum_{lmn}^{U} e^{i\boldsymbol{k}\cdot(\boldsymbol{R}_{lmn}^{p}-\boldsymbol{R}_{l'm'n'}^{p'})} \langle \varphi^{p'}, \boldsymbol{R}_{l'm'n'}^{p'} | \hat{H} | \varphi^{p}, \boldsymbol{R}_{lmn}^{p} \rangle \qquad \text{(B.9)}$$

$$\langle \Phi_{\boldsymbol{k}}^{p'} | \Phi_{\boldsymbol{k}}^{p} \rangle = \frac{1}{U} \sum_{l'm'n'}^{U} \sum_{lmn}^{U} e^{i\boldsymbol{k}\cdot(\boldsymbol{R}_{lmn}^{p}-\boldsymbol{R}_{l'm'n'}^{p'})} \langle \varphi^{p'}, \boldsymbol{R}_{l'm'n'}^{p'} | \varphi^{p}, \boldsymbol{R}_{lmn}^{p} \rangle \qquad \text{(B.10)}$$

Both sums in each matrix element run over every unit cell of the crystal. If one chooses a particular set of values of $l'm'n'$ and then executes the other sum over lmn, it gives the same as if another set of values of $l'm'n'$ had been chosen due to the periodicity of the crystal. It does not matter which value is chosen and all choices of $l'm'n'$ give the same contribution to the matrix element, so that the matrix element contains U equal terms. Thus, $l' = 0$, $m' = 0$ and $n' = 0$ can be chosen and the factor of $\frac{1}{U}$ is annihilated

$$\hat{\mathsf{H}}_{pp'} = \langle \Phi_{\boldsymbol{k}}^{p'} | \hat{H} | \Phi_{\boldsymbol{k}}^{p} \rangle = \sum_{lmn}^{U} e^{i\boldsymbol{k}\cdot\left(\boldsymbol{R}_{lmn}^{p}-\boldsymbol{R}_{000}^{p'}\right)} \langle \varphi^{p'}, \boldsymbol{R}_{000}^{p'} | \hat{H} | \varphi^{p}, \boldsymbol{R}_{\boldsymbol{lmn}}^{\boldsymbol{p}} \rangle \qquad \text{(B.11)}$$

$$\hat{\mathsf{S}}_{pp'} = \langle \Phi_{\boldsymbol{k}}^{p'} | \Phi_{\boldsymbol{k}}^{p} \rangle = \sum_{lmn}^{U} e^{i\boldsymbol{k}\cdot\left(\boldsymbol{R}_{lmn}^{p}-\boldsymbol{R}_{000}^{p'}\right)} \langle \varphi^{p'}, \boldsymbol{R}_{000}^{p'} | \varphi^{p}, \boldsymbol{R}_{\boldsymbol{lmn}}^{\boldsymbol{p}} \rangle \qquad \text{(B.12)}$$

From these equations the matrix elements can in principle be obtained and the eigenvalue problem solved for each value of $\boldsymbol{k}$ within the first Brillouin Zone (BZ) in order to obtain the band structure. However, if one does not have explicit expressions for the wave functions another approach has to be taken. One way is to use the tight binding method to calculate certain properties of the structure in question treating the matrix elements as fitting parameters. The calculation can then be fitted to experimental data (empirical tight binding) or to other more accurate calculations.

One task still remains for Eqn. B.4 to represent a physical wave function. The function has to be normalized, i.e., one must require that the function obeys

$$\langle \Psi_{j\boldsymbol{k}} | \Psi_{j\boldsymbol{k}} \rangle = \sum_{p,p'}^{N} c_{j}^{p}(\boldsymbol{k})^{*} c_{j}^{p'}(\boldsymbol{k}) \langle \Phi_{\boldsymbol{k}}^{p} | \Phi_{\boldsymbol{k}}^{p'} \rangle = \sum_{p,p'}^{N} c_{j}^{p}(\boldsymbol{k})^{*} c_{j}^{p'}(\boldsymbol{k}) \hat{\mathsf{S}}_{pp'} = 1 \qquad \text{(B.13)}$$

Or in matrix form

$$\boldsymbol{c}_{j}^{\dagger} \cdot \hat{\mathsf{S}} \cdot \boldsymbol{c}_{j} = 1 \qquad \text{(B.14)}$$

which constitutes the normalization condition for the eigenvectors. The eigenvector and the overlap matrix are of course all $\boldsymbol{k}$ dependent.

In the equations above no approximations are made. The crystal wave function is written as a linear combination of atomic orbitals, but this is not an approximation since the atomic orbitals constitute a complete set. The expressions for the matrix elements though, contain as many terms as there are unit cells in the crystal, i.e., infinitely many. But since the interaction

between atoms decreases rapidly when the distance between them increases, contributions to the matrix elements from atoms separated by more than a few nearest neighbour distances can be neglected. Often only nearest neighbours are included in the calculation but of course one is free to choose the number of nearest neighbours to include.

Another approximation which is frequently made is to completely ignore the overlap and simply put the overlap matrix equal to the unit matrix. In this way the matrix problem to be solved becomes

$$\hat{\mathsf{H}} \cdot \boldsymbol{c}_j = E_j(\boldsymbol{k})\boldsymbol{c}_j \tag{B.15}$$

i.e., a standard eigenvalue problem which is easier and faster to solve. This approximation is valid if the overlap matrix elements are small, i.e., if the atomic orbitals are strongly localized.

In the case of graphene it is the π electrons which are most interesting. This is because the π electrons are free to move in contrast to the other electrons which participate in covalent bonding and are therefore strongly localized. The π electrons therefore constitute the major contribution to the electrical and the optical properties of graphene. Therefore, in Eqn. B.1, the sum over p would be a sum over π orbitals only.

Appendix C

Graphene two band model

By applying the TB model in its simplest version to pure graphene a simple model which shows the most important features of graphene can be made. In this model the overlap is ignored and only nearest neighbour interactions are considered. The graphene lattice consists of two interpenetrating triagonal sub lattices which are called A and B in the following. Atoms belonging to the A lattice are also identified as A and similar for atoms belonging to the B lattice. Each atom has three nearest neighbours of the other type, i.e., an A atom has three nearest neighbours which are B atoms. In Fig. C.1(a) a graphene sheet is shown. The red atoms constitute the A sub lattice and the blue atoms constitute the B sub lattice. The set of lattice vectors shown is the set belonging to the A sub lattice. A similar set belongs to the B sub lattice. The shaded box shows the two atom unit cell of the graphene lattice. The total graphene sheet can be described as a triagonal lattice with a two atom basis. The lattice vectors of the graphene lattice is given by

$$\boldsymbol{a}_1 = \left(\frac{\sqrt{3}}{2}, \frac{1}{2} \right) a_0, \qquad \boldsymbol{a}_2 = \left(\frac{\sqrt{3}}{2}, -\frac{1}{2} \right) a_0 \tag{C.1}$$

where $a_0 = 2.46\,\text{Å}$ is the graphene lattice constant. Since there are two atoms in the unit cell, there are two Bloch functions. One for the A atoms and one for the B atoms. Thus, the matrix elements of the Hamiltonian matrix are given by

$$\langle \Phi^A | \hat{H} | \Phi^A \rangle = \langle \Phi^B | \hat{H} | \Phi^B \rangle = E_0 \tag{C.2}$$

$$\langle \Phi^A | \hat{H} | \Phi^B \rangle = \langle \Phi^B | \hat{H} | \Phi^A \rangle^* = \gamma_{01} \left[e^{i\boldsymbol{k}\cdot\boldsymbol{r}_1} + e^{i\boldsymbol{k}\cdot\boldsymbol{r}_2} + e^{i\boldsymbol{k}\cdot\boldsymbol{r}_3} \right] = \gamma_{01} f_1(\boldsymbol{k}) \tag{C.3}$$

where $\boldsymbol{r}_i$ are the vectors which connect an A or B atom with its nearest neighbours. The transfer integral $\gamma_{01} = \langle \varphi^A(\boldsymbol{r}) | \hat{H} | \varphi^B(\boldsymbol{r} - \boldsymbol{r}_i) \rangle$ is the same for all i since all nearest neighbours obviously lie in the same distance from the center atom. The vectors $\boldsymbol{r}_i$ are given by

$$\boldsymbol{r}_1 = (\frac{1}{2\sqrt{3}}, \frac{1}{2})a_0, \qquad \boldsymbol{r}_2 = (\frac{1}{2\sqrt{3}}, -\frac{1}{2})a_0, \qquad \boldsymbol{r}_3 = (-1, 0)a_0 \tag{C.4}$$
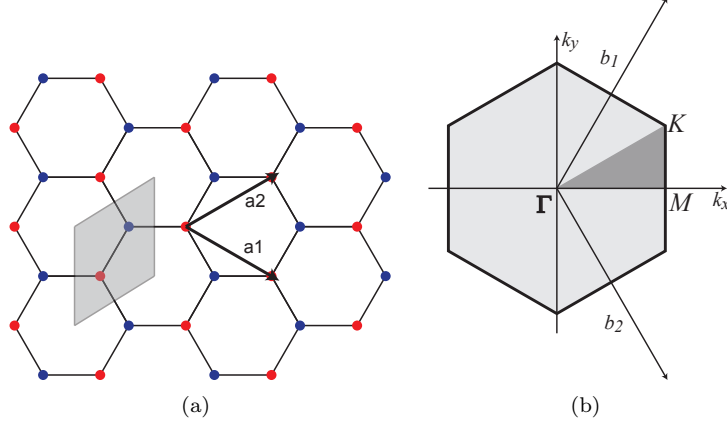
Figure C.1: (a) a graphene lattice and the two atom unit cell in graphene. Atoms belonging to different sub lattices are colored in different colors. (b) the Brillouin zone of graphene. The shaded area is the irreducible BZ.

and the exponential factor $f_1(\boldsymbol{k})$ in Eqn. C.3 is therefore found to be

$$f_1(\boldsymbol{k}) = e^{-ik_x a_0/\sqrt{3}} + 2e^{ik_x a_0/(2\sqrt{3})}\cos(k_y a_0/2) \tag{C.5}$$

In order to calculate the band structure the reciprocal lattice vectors has to be known. These are calculated from the requirement that $e^{i\boldsymbol{a}_i\cdot\boldsymbol{b}_j} = 2\pi\delta_{ij}$ from which it follows that $\boldsymbol{a}_i \cdot \boldsymbol{b}_j = 1$. The reciprocal lattice vectors are found to be

$$\boldsymbol{b}_1 = \left(\frac{1}{\sqrt{3}}, 1\right)\frac{2\pi}{a_0}, \qquad \boldsymbol{b}_2 = \left(\frac{1}{\sqrt{3}}, -1\right)\frac{2\pi}{a_0} \tag{C.6}$$

From the reciprocal lattice vectors the first Brillouin zone can be constructed. This is done by constructing the Wigner-Seitz cell from the reciprocal lattice vectors. The first Brillouin zone is shown in Fig. C.1(b). The band structure is calculated by evaluating the eigenvalues of the Hamiltonian matrix for $\boldsymbol{k}$ values on the path $\Gamma - M - K - \Gamma$. Setting $E_0 = 0$ (it only causes a shift of the eigenvalues) the eigenvalues are given by

$$\begin{vmatrix} -E & -\gamma f_1(\boldsymbol{k}) \\ -\gamma f_1^*(\boldsymbol{k}) & -E \end{vmatrix} = E^2 - \gamma^2 \left|f(\boldsymbol{k})\right|^2 = 0 \tag{C.7}$$

so that the eigenvalues are given by $E(\boldsymbol{k}) = \pm\gamma\left|f_1(\boldsymbol{k})\right|$. From this it is seen that if $\left|f_1(\boldsymbol{k})\right| = 0$ for some $\boldsymbol{k}$ there will be no band gap. $\left|f_1(\boldsymbol{k})\right|^2$ is given by

$$\left|f_1(\boldsymbol{k})\right|^2 = 1 + 4\cos^2\left(k_y\frac{a_0}{2}\right) + 4\cos\left(k_y\frac{a_0}{2}\right)\cos\left(k_x\frac{\sqrt{3}a_0}{2}\right) \tag{C.8}$$

The K point in reciprocal space lies at $(\frac{2\pi}{\sqrt{3}a_0}, \frac{2\pi}{3a_0})$ and inserting this into the expression for $|f_1(\boldsymbol{k})|^2$ one gets

$$|f_1(\boldsymbol{K})|^2 = 1 + 4\cos^2\frac{\pi}{3} + 4\cos\frac{\pi}{3}\cos\pi = 0 \qquad \text{(C.9)}$$

so that the bands meet in the K point. This point is called the Dirac Point. By doing a second order expansion of the expression for the energy around the K point further properties of graphene can be derived[7], i.e., putting $\boldsymbol{k} = \boldsymbol{K} + \boldsymbol{q}$ where $|\boldsymbol{q}| \ll \boldsymbol{K}$ and using the addition formulas for $\cos x$ one obtains

$$E(\boldsymbol{q}) \approx v\,|\boldsymbol{q}| \qquad \text{(C.10)}$$

where $v = \sqrt{3}\gamma a_0/2$. In the usual case one has $E(\boldsymbol{q}) = |\boldsymbol{q}|^2/(2m) = v(\boldsymbol{q})\,|\boldsymbol{q}|$ so that the velocity depends on the wave vector $\boldsymbol{q}$. In the case of graphene in the vicinity of the $\boldsymbol{K}$ point the velocity does not depend on the wave vector. The velocity of electrons near the $\boldsymbol{K}$ point is equal to the Fermi velocity $v_F = 10^6 m/s$[7] so that, still near the $\boldsymbol{K}$ point,

$$E(\boldsymbol{q}) \approx v_F\,|\boldsymbol{q}| \qquad \text{(C.11)}$$

The impact of this result is that the velocity of electrons near the Dirac point does not depend on energy or momentum, but is equal to the Fermi velocity. The Fermi velocity in graphene is $\sim c/300$, where c is the speed of light.

Appendix D

The Fourier series and Fourier transform

In this appendix Fourier series and Fourier transforms are explained, in order to give the reader at least some background information on this subject [20]. The central theme in Fourier analysis is to break complicated periodic functions into simpler periodic functions that are easier to understand. For example, a Fourier series is a sum of sines and cosines which by themselves are easy to understand. Since these functions constitute a complete orthogonal set, any function can be build from sines and cosines. Thus, a complicated function can be represented by a Fourier series, but the individual pieces are by themselves easy to deal with. A Fourier series of an arbitrary periodic function $f(x) = f(x + L)$ can be written in the following way

$$f(x) = \sum_n \tilde{f}_n e^{i2\pi nx/L} \tag{D.1}$$

where instead of sines and cosines the complex exponential function is used. The coefficients are complex quantities and the summation ranges from $n = -\infty$ to $n = \infty$. The function is periodic with period L as one can easily see by writing

$$f(x + L) = \sum_n \tilde{f}(k) e^{i2\pi n(x+L)/L} = \sum_n \tilde{f}(k) e^{i2\pi nx/L} e^{i2\pi n} = f(x) \tag{D.2}$$

since $e^{i2\pi n} = 1$. It should be stressed that the function $f(x)$ need to be periodic in order for the Fourier series to converge. Non periodic functions are the domain of Fourier transforms and will be dealt with later. Now, in order to determine the Fourier coefficients both sides of Eqn. D.1 are multiplied by $e^{-i2\pi mx/L}$ and integrated from $x = -L/2$ to $x = L/2$, since the complex exponential functions used here are orthogonal over this interval. Thus

$$\int_{-L/2}^{L/2} f(x)e^{-i2\pi mx/L}dx = \int_{-L/2}^{L/2} \sum_n \tilde{f}_n e^{i2\pi(n-m)x/L}dx = \sum_n \tilde{f}_n \int_{-L/2}^{L/2} e^{i2\pi(n-m)x/L}dx$$

$$= \sum_n \tilde{f}_n \frac{L\sin\left[(m-n)\pi\right]}{\pi(m-n)} = L\sum_n \tilde{f}_n \delta_{mn} = L\tilde{f}_m \quad \text{(D.3)}$$

Thus, the Fourier coefficients of Eqn. D.1 are given by

$$\tilde{f}_n = \frac{1}{L}\int_{-L/2}^{L/2} f(x)e^{-i2\pi nx/L}dx \quad \text{(D.4)}$$

It should be noted that the complex exponentials are orthogonal over other intervals as well, for example the interval $[-L, L]$. Choosing another interval will of course not make a difference to the Fourier coefficients. This is due to the periodicity of all involved quantities.

Now, one could wonder what would happen as the period of $f(x)$ goes to infinity. Introducing $k_n = 2\pi n/L$ and $\Delta k = 2\pi/L$ Eqn. D.1 becomes

$$f(x) = \frac{L}{2\pi}\sum_n \tilde{f}_n e^{ik_n x}\Delta k \quad \text{(D.5)}$$

As L becomes very large, $\Delta k \to 0$ and the k_n's become infinitely closely spaced. Thus, the above expression looks like the Riemann definition of the integral and one can write in the limit where $L \to \infty$

$$f(x) = \frac{L}{2\pi}\int_{-\infty}^{\infty} \tilde{f}(k)e^{ikx}dk \quad \text{(D.6)}$$

This is the Fourier transform of $f(x)$ and it is the generalization of the Fourier series Eqn. D.1 to non-periodic functions. In order to determine the Fourier coefficients one proceeds as in the case of Fourier series by multiplying both sides of the equation by $e^{-ik'x}$ and integrating with respect to x from $-\infty$ to ∞

$$\int_{-\infty}^{\infty} f(x)e^{-ik'x}dx = \frac{L}{2\pi}\int_{-\infty}^{\infty} \tilde{f}(k)\left[\int_{-\infty}^{\infty} e^{i(k-k')x}dx\right]dk \quad \text{(D.7)}$$

The quantity in brackets is equivalent to the Dirac Delta function multiplied by 2π (actually, it is one of the definitions of the Dirac Delta function) so that

$$\int\limits_{-\infty}^{\infty} f(x)e^{-ik'x}dx = L\int\limits_{-\infty}^{\infty} \tilde{f}(k)\delta(k-k')dk = L\tilde{f}(k') \tag{D.8}$$

The Fourier coefficients are then given by

$$\tilde{f}(k) = \frac{1}{L}\int\limits_{-\infty}^{\infty} f(x)e^{-ikx}dx \tag{D.9}$$

Eqn. D.6 and Eqn. D.9 constitute a Fourier transform pair. By combining these two equations one obtains the Fourier integral theorem as follows

$$f(x) = \frac{1}{2\pi}\int\limits_{-\infty}^{\infty}\int\limits_{-\infty}^{\infty} f(x')e^{ik(x-x')}dx'dk \tag{D.10}$$

Fourier transforms generalizes to more than one dimension in the obvious way

$$f(\boldsymbol{x}) = \frac{L^n}{(2\pi)^n}\int \tilde{f}(\boldsymbol{k})e^{i\boldsymbol{k}\cdot\boldsymbol{x}}d^n k \tag{D.11}$$

$$\tilde{f}(\boldsymbol{k}) = \frac{1}{L^n}\int f(\boldsymbol{x})e^{-\boldsymbol{k}\cdot\boldsymbol{x}}d^n x \tag{D.12}$$

where $\boldsymbol{x}$ and $\boldsymbol{k}$ are n-dimensional vectors. The Fourier coefficients can be chosen with an arbitrary factor in front, as long as this is compensated for in the Fourier transform. This will of course change the Fourier coefficients but not the Fourier transform. The factor of $1/(2\pi)$ above can be split between the two equations as follows

$$f(\boldsymbol{x}) = \frac{L^n}{(2\pi)^{n/2}}\int \tilde{f}(\boldsymbol{k})e^{i\boldsymbol{k}\cdot\boldsymbol{x}}d^n k \tag{D.13}$$

$$\tilde{f}(\boldsymbol{k}) = \frac{1}{L^n(2\pi)^{n/2}}\int f(\boldsymbol{x})e^{-\boldsymbol{k}\cdot\boldsymbol{x}}d^n x \tag{D.14}$$

An important property of a Fourier transformation is that it is a unitary transformation. This means that it preserves the inner product so that the inner product of a function is equal to the inner product of its Fourier transform, i.e.

$$\int\limits_{-\infty}^{\infty} |f(x)|^2\, dx = \int\limits_{-\infty}^{\infty} \left|\tilde{f}(k)\right|^2 dk \tag{D.15}$$

This relation is also known as Parseval's theorem. It has the important property that energy is conserved under a Fourier transform.

Bibliography

[1] R. Petersen and T. G. Pedersen. Quasiparticle properties of graphene antidot lattices. Submitted.

[2] René Petersen. Tight-binding based modelling of graphene antidot structures. Technical report, Institute for Physics and Nanotechnology, Aalborg University, Denmark, 2009. `www.repetit.dk`.

[3] Xu Du, Ivan Skachko, Anthony Barker, and Eva Y. Andrei. Approaching ballistic transport in suspended graphene. *Nat. Nanotechnol.*, 3:491, 2008.

[4] Andrey K. Geim and Allan H. MacDonald. Graphene: Exploring carbon flatland. *Phys. Today*, 2007.

[5] A. K. Geim and K. S. Novoselov. The rise of graphene. *Nat. Mat.*, 6:183, 2007.

[6] K. S. Novoselov, D. Jiang, F. Schedin, T. J. Booth, V. V. Khotkevich, S. V. Morozov, and A. K. Geim. Two-dimensional atomic crystals. *Proc. Natl. Acad. Sci USA*, 102:10451, 2005.

[7] A. H. Castro Neto, F. Guinea, N. M. R. Peres, K. S. Novoselov, and A. K. Geim. The electronic properties of graphene. *arxiv.org:0709.1163v2 [cond. mat]*, 2008.

[8] Vernica Barone, Oded Hod, and Gustavo E. Scuseria. Electronic structure and stability. *Nano. Lett.*, 6:2748–2754, 2008.

[9] Melinda Y. Han, Barbados Özyilmaz, Yanbo Zhang, and Philip Kim. Energy band-gap engineering of graphene nanoribbons. *Phys. Rev. Lett.*, 98:206805, 2007.

[10] T. G. Pedersen, C. Flindt, J. Pedersen, A. P. Jauho, N. A. Mortensen, and K. Pedersen. Optical properties of graphene antidot lattices. *Phys. Rev. B*, 77:245431, 2008.

[11] T. G. Pedersen, C. Flindt, J. Pedersen, N. A. Mortensen, A. P. Jauho, and K. Pedersen. Graphene antidot lattices: Designed defects and spin cubits. *Phys. Rev. Lett.*, 100:136804, 2008.

[12] A. Grüneis, C. Attaccalite, L. Wirtz, H. Shiozawa, R. Saito, T. Pichler, and A. Rubio. Tight-binding description of the quasiparticle dispersion of graphite and few-layer graphene. *Phys. Rev. B*, 78:205425, 2008.

[13] J. Eroms and D. Weiss. Weak localications and transport gap in graphene antidot lattices. *arXiv.org:0901.0840v1 [cond-mat.mes-hall]]*, 2009.

[14] T. G. Pedersen, A.-P. Jauho, and K. Pedersen. Nonlocal conductivity and screening in gapped graphene. Unpublished.

[15] Robert S. Knox. *Theory of Excitons.* Academic Press, 1963.

[16] Frank Jensen. *Introduction to Computational Chemistry.* Wiley, 1999.

[17] Lionel Salem. *The Molecular Orbital Theory of Conjugated Systems.* W. A. Benjamin, Inc, 1966.

[18] J. P. Dahl. *Introduction to the Quantum World of Atoms and Molecules.* World Scientific, 2001.

[19] C. Kittel. *Introduction to Solid State Physics.* John Wiley and sons, 2003. 0-471-41526-X.

[20] Donald A. McQuarrie. *Mathematical Methods for Scientists and Engineers.* University Science Books, 2003.